Constitutive modeling of initially stressed solids from stress data using mechanics-informed neural networks

Yiwei Duan[a], Artur L. Gower[b], Wenchang Tan[a,*], Guo-Yang Li[a,*]

[a]*School of Mechanics and Engineering Science, Peking University, Beijing 100871, PR China*
[b]*School of Mechanical, Aerospace and Civil Engineering, University of Sheffield, Sheffield, UK*

Abstract

Predicting how initial stress alters the mechanical behavior of soft materials is essential for applications ranging from personalized surgical planning to soft robotics. In biomedical contexts, residual stresses and prestresses–such as those found in the cornea, skin, or arterial walls–significantly influence how tissues deform, heal, and respond to intervention. Accurate predictions, for example after LASIK surgery or vascular stenting, require constitutive models that account for initial stress. An additional challenge is that each tissue exhibits a unique mechanical response that should be characterized prior to intervention. Here, we introduce a mechanics-informed neural network (MINN) framework for constitutive modeling of initially stressed elastic solids from stress and deformation data. Our approach embeds the physical constraints associated with initially stressed elasticity–including initial stress compatibility and initial stress reference independence–into the network architecture. This enables standard strain-energy functions, such as the widely used Holzapfel–Gasser–Ogden model, to be extended to account for initial stress. As a proof-of-concept, we design an experiment to mimic the corneal deformation under varying intraocular pressure. Using non-invasive guided wave measurements, we identify constitutive parameters directly in the loaded configuration and validate the resulting model by predicting corneal deformations under altered loading conditions. These results demonstrate the feasibility of constitutive modeling directly from stress data and establish a framework for patient-specific biomechanical modeling and preoperative planning.

Keywords: Initially stressed solids, Constitutive modeling, Mechanics-informed neural networks, Acoustoelasticity, Soft biological tissues

*Corresponding author.
Email addresses: tanwch@pku.edu.cn (Wenchang Tan), lgy@pku.edu.cn (Guo-Yang Li)

1. Introduction

Biological tissues are rarely stress-free. Residual and prestresses–arising from growth (Fung, 1991), remodeling, or sustained physiological loads (Chuong and Fung, 1986; Hoger, 1986)–affect how organs deform, transmit forces (Zheng et al., 2024), heal, and respond to surgical intervention. These internal stress fields are significant in soft tissues such as the cornea, skin, and arterial walls, where small changes in geometry or stiffness can change vision, wound healing, or cardiovascular health. For example, in the eye, the shape of the cornea after LASIK surgery critically depends on the state of internal stress prior to ablation and the mechanical response of the cornea. Similarly, surgical planning for skin incisions and scar minimization benefits from understanding local stress distributions, while stent placement in arteries affects long-term vessel remodeling through changes in wall stress. For this reason, accurate prediction of tissue mechanics often requires constitutive models that explicitly account for the underlying stress state.

Despite this importance, conventional constitutive models typically ignore initial stress or assume access to an idealized, stress-free configuration, which is rarely available for biological tissues. Furthermore, tissues vary considerably from one individual to another, making it essential to tailor models to each patient. This motivates a shift toward subject-specific constitutive modeling, in which the constitutive response is identified directly from the loaded configuration of a given tissue.

The need for constitutive models that account for initial stress has motivated extensive research into the mechanics of prestressed solids (Kang et al., 2025). Initial stress refers to any internal stress within an elastic material (Fung, 1990; Hoger, 1996). It may arise from applied loads or exist even in the absence of external forces, in which case it is referred to as residual stress (Chuong and Fung, 1986; Hoger, 1986; Merodio et al., 2013; Todd et al., 1999). In recent decades, advances in the biomechanics of soft tissues have driven substantial progress in the modeling and characterization of initially stressed materials (Holzapfel and Ogden, 2003; Mukherjee et al., 2022; Mukherjee and Ravindran, 2024; Ogden and Singh, 2014), with the ultimate aim of improving healthcare diagnostics and treatment (Li et al., 2024).

A common approach to model the response of a solid under initial stress $\boldsymbol{\tau}$ is to assume there exists a virtual stress-free state $\mathcal{B}_0$ (Johnson and Hoger, 1995), as shown in Fig. 1a. The initial stress is then created through the deformation $\boldsymbol{F}_1$, and then a further elastic deformation $\boldsymbol{F}$ is used to couple elastic deformations with the initial stress. Gower et al. (2015) used this approach to deduce an explicit potential energy $W(\boldsymbol{F}, \boldsymbol{\tau})$ which is equivalent to an initially stressed neo-Hookean energy. Agosti et al. (2018) extended this approach to deduce an initially stressed Mooney-Rivlin potential energy. Over the past few decades, this method has also been applied to elastoplastic materials, viscoelasticity, porous materials, and polymers (Chester and Anand, 2011; Du et al., 2018, 2019; Molinari et al., 2022; Rausch and Kuhl, 2013; Reina and Conti, 2017; Reina et al., 2018; Sadik and Yavari, 2024; Skalak et al., 1996; Soyarslan and Bargmann, 2016; Yang et al., 2023; Yavari and Sozio, 2023). A limitation of this approach is that extending it to more realistic constitutive models requires solving a difficult nonlinear inverse problem relating the initial stress to the unknown virtual stress-free configuration. As a result, analytical solutions are available only for a limited number of constitutive models (Ciarletta et al., 2016; Dorfmann and Ogden, 2021; Melnikov et al., 2021; Merodio and Ogden, 2016; Shariff et al., 2017, 2019).

An alternative is to directly deduce potential energies $W := W(\boldsymbol{F}, \boldsymbol{\tau})$ which are explicit functions of $\boldsymbol{\tau}$ without considering a stress-free configuration (Ciarletta et al., 2016; Dorfmann and Ogden, 2021; Melnikov et al., 2021; Merodio and Ogden, 2016; Shariff et al., 2017, 2019). The strain energy density function is explicitly formulated using invariants derived from $\boldsymbol{\tau}$ and $\boldsymbol{F}$ (Gower et al., 2015, 2017, 2025). However, only relatively simple forms of $W(\boldsymbol{F}, \boldsymbol{\tau})$ have been established, owing to the difficulty of simultaneously satisfying these physical constraints and representing complex ma-

terial behavior. This limitation becomes particularly restrictive for biological tissues, which often exhibit strong anisotropy and nonlinear responses (see Sec. 3 for a discussion). This motivates the development of more general frameworks for constructing constitutive models of initially stressed materials.

Data-driven approaches have recently emerged as a powerful alternative for constitutive modeling, enabling complex material responses to be learned directly from data without requiring an explicit analytical form of the strain-energy function. For stress-free materials, such methods have been successfully applied to learn hyperelastic constitutive models while preserving important physical properties such as material symmetry, objectivity, and thermodynamic consistency (Brodnik et al., 2023; Li et al., 2025; Prume et al., 2023; Wu et al., 2025). Extending these approaches to initially stressed solids is considerably more challenging. Unlike conventional constitutive models, the initial stress itself enters the strain-energy function and must therefore be characterized as an additional constitutive variable. Consequently, the learned constitutive model must not only reproduce the observed mechanical response but also satisfy the physical constraints associated with initially stressed elasticity, including initial stress compatibility and initial stress reference independence (Gower et al., 2017). Moreover, the availability of stress data becomes a fundamental requirement because the initial stress itself enters the constitutive model as an independent constitutive variable rather than merely a loading condition (Li et al., 2025; Thakolkaran et al., 2022).

Here, we present a mechanics-informed deep learning framework for constitutive modeling of initially stressed solids from stress and deformation data. The proposed architecture embeds the required physical constraints into the network design, allowing standard constitutive models, including the widely used Holzapfel–Gasser–Ogden model, to be extended to incorporate initial stress. The resulting framework provides a general approach for constructing constitutive models of initially stressed soft materials and biological tissues directly from stress and deformation data.

A remaining challenge is the acquisition of stress data required by the proposed framework. Unlike displacement and force measurements, internal stress fields are generally difficult to obtain experimentally. Recently, however, we developed Acoustoelastic Imaging (AEI), a non-destructive technique that reconstructs internal stress fields from shear-wave measurements without requiring prior knowledge of the constitutive model (Duan et al., 2026). In the present work, we show how stress fields obtained from AEI can be incorporated into the proposed constitutive framework, providing a pathway toward patient-specific constitutive modeling directly from loaded configurations. As a proof of concept, we demonstrate constitutive modeling of prestressed corneal phantoms and discuss its potential for patient-specific biomechanical characterization and surgical planning.

This paper is organised as follows. In Sec. 2, we present the key physical constraints for constitutive models of initially stressed solids and derive the corresponding expressions for the strain-energy density and stress. In Sec. 3, we describe the architecture and training procedure of the proposed MINN framework and show how the physical constraints are incorporated into the learning process. In Sec. 4, we implement the learned constitutive model within a finite element framework and evaluate its performance on benchmark problems, including incremental wave propagation and corneal deformation. In Sec. 5, we perform experiments on prestressed corneal phantoms and use Optical Coherence Tomography to identify constitutive parameters of initially stressed models. In Sec. 6, we discuss how initial stress can be obtained without prior knowledge of the material parameters and present an additional validation of the proposed framework. Finally, concluding remarks are provided in Sec. 7.

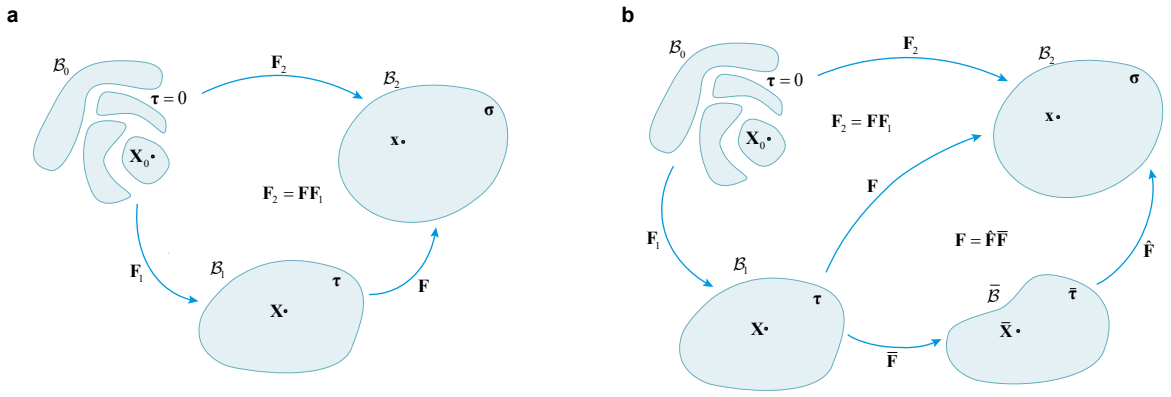


Figure 1: Configurations involved in the deformation of an initially stressed elastic solid. (a) Virtual stress-free configuration $\mathcal{B}_0$, initially stressed configuration $\mathcal{B}_1$ with initial stress $\boldsymbol{\tau}$, and current configuration $\mathcal{B}_2$ with Cauchy stress $\boldsymbol{\sigma}$. (b) Alternative reference configuration $\bar{\mathcal{B}}$ with corresponding initial stress $\bar{\boldsymbol{\tau}}$, illustrating the concept of initial stress reference independence (ISRI).

2. Constitutive modeling of initially stressed elastic solids

Below, we briefly summarize the equations required to describe the elastic response of initially stressed solids. For a more comprehensive review of the constitutive theory of initially stressed elastic solids, readers are referred to (Gower et al., 2015, 2017, 2025; Mukherjee et al., 2022; Shams et al., 2011).

2.1. Kinematics and stress

Consider a hyperelastic material with a prescribed initial Cauchy stress $\boldsymbol{\tau}$ in the reference configuration $\mathcal{B}_1$, from which subsequent deformations are measured. In the absence of body forces and under static equilibrium, the initial stress field satisfies

$$\operatorname{Div} \boldsymbol{\tau} = 0, \tag{1}$$

where Div denotes the divergence operator with respect to the configuration $\mathcal{B}_1$. Furthermore, in the absence of intrinsic couple stresses, the Cauchy stress tensor $\boldsymbol{\tau}$ is symmetric.

Now consider an elastic deformation that maps the material from $\mathcal{B}_1$ to a new configuration $\mathcal{B}_2$. The deformation is described by the mapping $\boldsymbol{x} = \boldsymbol{\chi}(\boldsymbol{X})$, where $\boldsymbol{x}$ denotes the position in $\mathcal{B}_2$ of a material point that occupied the position $\boldsymbol{X}$ in $\mathcal{B}_1$. The associated deformation gradient tensor $\boldsymbol{F}$ is given by $\boldsymbol{F} = \operatorname{Grad} \boldsymbol{\chi}$, where Grad denotes the gradient operator with respect to the reference configuration $\mathcal{B}_1$. From $\boldsymbol{F}$, the left and right Cauchy–Green deformation tensors are defined as

$$\boldsymbol{B} = \boldsymbol{F}\boldsymbol{F}^{\mathrm{T}}, \quad \boldsymbol{C} = \boldsymbol{F}^{\mathrm{T}}\boldsymbol{F}. \tag{2}$$

The Cauchy stress tensor in the deformed configuration $\mathcal{B}_2$ is denoted by $\boldsymbol{\sigma}$. In the absence of intrinsic couple stresses, $\boldsymbol{\sigma}$ is also symmetric.

2.2. The strain energy function

To account directly for modifications to the mechanical response induced by initial stress $\boldsymbol{\tau}$, we consider a strain-energy density function of the form $W = W(\boldsymbol{F}, \boldsymbol{\tau})$. In many soft tissues, however, fibers or other forms of structural anisotropy also contribute significantly to the mechanical response.

To incorporate these effects, we introduce the fiber orientation vector $\boldsymbol{M}$, which characterizes the fiber orientation in the reference configuration, and write the strain-energy density as

$$W = W\left(\boldsymbol{F},\ \boldsymbol{\tau},\ \boldsymbol{M}\right). \tag{3}$$

For materials that are not subject to internal constraints, such as incompressibility, the Cauchy stress tensor $\boldsymbol{\sigma}$ in the deformed configuration is given by

$$\boldsymbol{\sigma} = J^{-1}\boldsymbol{F}\frac{\partial W}{\partial \boldsymbol{F}}\left(\boldsymbol{F},\ \boldsymbol{\tau},\ \boldsymbol{M}\right), \tag{4}$$

where $J = \det \boldsymbol{F}$. Evaluating Eq. (4) in the reference configuration, $\boldsymbol{F} = \boldsymbol{I}$, yields

$$\boldsymbol{\tau} = \frac{\partial W}{\partial \boldsymbol{F}}\left(\mathbf{I},\ \boldsymbol{\tau},\ \boldsymbol{M}\right), \tag{5}$$

where $\mathbf{I}$ denotes the identity tensor.

For incompressible materials, the Cauchy stress tensor is given by

$$\boldsymbol{\sigma} = \boldsymbol{F}\frac{\partial W}{\partial \boldsymbol{F}}\left(\boldsymbol{F},\ \boldsymbol{\tau},\ \boldsymbol{M}\right) - p\mathbf{I}, \quad \text{with} \quad J = 1, \tag{6}$$

where p is a Lagrange multiplier associated with the incompressibility constraint.

2.3. Invariant formulation

Assuming that the strain-energy density W depends on only on the initial stress $\boldsymbol{\tau}$, the deformation gradient $\boldsymbol{F}$, and the fiber orientation vector $\boldsymbol{M}$, it follows (Gower et al., 2017; Mukherjee et al., 2022; Shams et al., 2011) that W can be expressed in terms of the following 18 invariants:

$$\begin{aligned}
&I_1 = \mathrm{tr}\boldsymbol{C}, \quad I_2 = \frac{1}{2}\left[(\mathrm{tr}\boldsymbol{C})^2 - \mathrm{tr}\left(\boldsymbol{C}^2\right)\right], \quad I_3 = \det\left(\boldsymbol{C}\right), \quad I_{\tau_1} = \mathrm{tr}\boldsymbol{\tau}, \quad I_{\tau_2} = \mathrm{tr}\left(\boldsymbol{\tau}^2\right),\\
&I_{\tau_3} = \mathrm{tr}\left(\boldsymbol{\tau}^3\right), \quad I_6 = \mathrm{tr}\left(\boldsymbol{\tau}\boldsymbol{C}\right), \quad I_7 = \mathrm{tr}\left(\boldsymbol{\tau}\boldsymbol{C}^2\right), \quad I_8 = \mathrm{tr}\left(\boldsymbol{\tau}^2\boldsymbol{C}\right), \quad I_9 = \mathrm{tr}\left(\boldsymbol{\tau}^2\boldsymbol{C}^2\right),\\
&I_4 = \boldsymbol{M}\cdot\boldsymbol{C}\boldsymbol{M}, \quad I_5 = \boldsymbol{M}\cdot\boldsymbol{C}^{\mathbf{2}}\boldsymbol{M}, \quad I_{\tau 4} = \boldsymbol{M}\cdot\boldsymbol{\tau}\boldsymbol{M}, \quad I_{\tau 5} = \boldsymbol{M}\cdot\boldsymbol{\tau}^2\boldsymbol{M},\\
&I_{14} = \boldsymbol{M}\cdot\boldsymbol{\tau}\boldsymbol{C}\boldsymbol{M}, \quad I_{15} = \boldsymbol{M}\cdot\boldsymbol{\tau}\boldsymbol{C}^{\mathbf{2}}\boldsymbol{M}, \quad I_{16} = \boldsymbol{M}\cdot\boldsymbol{\tau}^2\boldsymbol{C}\boldsymbol{M}, \quad I_{17} = \boldsymbol{M}\cdot\boldsymbol{\tau}^2\boldsymbol{C}^{\mathbf{2}}\boldsymbol{M}.
\end{aligned} \tag{7}$$

The subscripts 10–13 and 18 are omitted because invariants involving the initial stress are denoted separately using the subscript τ. Among the 18 invariants listed above, at most eleven are mutually independent (Shariff and Merodio, 2020). Motivated by this observation, the present formulation retains the following eleven invariants: I_1, I_2, I_3, I_4, I_5, I_6, I_7, I_9, I_{τ_1}, I_{τ_2}, and I_{τ_3}. The remaining invariants are not included as additional constitutive inputs in the present model. This represents a reduced invariant formulation, and the selected set is not unique. For isotropic materials, the fiber-related invariants I_4 and I_5 are omitted, as there is no preferred fiber direction. The initial-stress invariants I_{τ_1}, I_{τ_2}, and I_{τ_3} enter the strain-energy representation but do not contribute directly to the stress tensor (see Eq. (9)) because their derivatives with respect to the right Cauchy–Green deformation tensor vanish.

To express the stress tensor in terms of the invariants, we write

$$\boldsymbol{\sigma} = \boldsymbol{F}\sum_{i\in\mathcal{I}} W_i\frac{\partial I_i}{\partial \boldsymbol{F}}, \tag{8}$$

or, equivalently,

$$\begin{aligned}
\boldsymbol{\sigma} = {}& 2W_1\boldsymbol{B} + 2W_2\left(I_1\boldsymbol{B} - \boldsymbol{B}^2\right) + 2W_3I_3\mathbf{I} + 2W_6\boldsymbol{\Sigma} + 2W_7\left(\boldsymbol{\Sigma}\boldsymbol{B} + \boldsymbol{B}\boldsymbol{\Sigma}\right) + 2W_9\left(\boldsymbol{\Pi}\boldsymbol{B} + \boldsymbol{B}\boldsymbol{\Pi}\right)\\
&+ 2W_4\boldsymbol{F}\boldsymbol{G}\boldsymbol{F}^T + 2W_5\left(\boldsymbol{F}\boldsymbol{G}\boldsymbol{F}^T\boldsymbol{B} + \boldsymbol{B}\boldsymbol{F}\boldsymbol{G}\boldsymbol{F}^T\right),
\end{aligned} \tag{9}$$

where $W_i = \partial W/\partial I_i$, $\boldsymbol{G} = \boldsymbol{M}\otimes\boldsymbol{M}$, $\boldsymbol{\Sigma} = \boldsymbol{F}\boldsymbol{\tau}\boldsymbol{F}^{\mathrm{T}}$, and $\boldsymbol{\Pi} = \boldsymbol{F}\boldsymbol{\tau}^2\boldsymbol{F}^{\mathrm{T}}$. For solids without fibers, the above expressions reduce to the isotropic case by setting $W_4 = W_5 = 0$.

2.4. ISRI and ISC conditions

For strain-energy functions that depend explicitly on the initial stress $\boldsymbol{\tau}$, an additional constraint is required to ensure that the model represents the same material undergoing purely elastic deformations (Gower et al., 2017, 2025), i.e., in the absence of growth or other inelastic processes. To simplify the discussion, we omit the fiber direction $\boldsymbol{M}$; see (Mukherjee et al., 2022) for how ISRI can be naturally extended to materials with fibers.

In summary, the energy of the configuration $\mathcal{B}_2$, shown in Fig. 1b, must be identical whether evaluated with respect to the reference configuration $\mathcal{B}_1$ or with respect to an arbitrary intermediate configuration $\bar{\mathcal{B}}$, which is related to $\mathcal{B}_1$ through a deformation gradient $\bar{\boldsymbol{F}}$. This requirement leads to the initial stress reference independence (ISRI) condition (Gower et al., 2017):

$$W\left(\boldsymbol{F}, \boldsymbol{\tau}\right) = W\left(\hat{\boldsymbol{F}}, \bar{\boldsymbol{\tau}}\right), \tag{10}$$

where $\bar{\boldsymbol{\tau}} = \boldsymbol{\sigma}\left(\bar{\boldsymbol{F}}, \boldsymbol{\tau}\right)$ and $\boldsymbol{F} = \hat{\boldsymbol{F}}\bar{\boldsymbol{F}}$.

When $\bar{\boldsymbol{F}} = \mathbf{I}$, Eq. (10) reduces to:

$$W\left(\hat{\boldsymbol{F}}, \boldsymbol{\tau}\right) = W\left(\hat{\boldsymbol{F}}, \boldsymbol{\sigma}\left(\mathbf{I}, \boldsymbol{\tau}\right)\right). \tag{11}$$

It is evident that if

$$\boldsymbol{\sigma}\left(\mathbf{I}, \boldsymbol{\tau}\right) = \boldsymbol{\tau}, \tag{12}$$

then Eq. (11) holds for arbitrary $\boldsymbol{\tau}$. This requirement is referred to as the initial stress compatibility (ISC) condition.

The theoretical interpretation and scope of ISRI have recently been further discussed in the literature. Ogden (Ogden, 2023) raised concerns regarding the treatment of changes in reference configuration underlying the formulation of ISRI in Gower et al. (Gower et al., 2017). In a subsequent response, Gower et al. (Gower et al., 2025) clarified the distinction between two types of constitutive functions. For type-1 functions, $\tilde{W}(\boldsymbol{F}, \boldsymbol{\tau})$ represents a family of different materials sharing a fixed reference configuration, for which ISRI is not required. In contrast, type-2 functions $W(\boldsymbol{F}, \boldsymbol{\tau}, \boldsymbol{X})$ describe a single material associated with a family of differently stressed reference configurations, for which the authors retain ISRI as a necessary consequence of classical elasticity. This distinction is particularly relevant to the present formulation and motivates the assessment of ISRI for the learned constitutive model presented below.

3. Mechanics-informed learning of constitutive models for initially stressed solids

We adopt a supervised learning framework to construct constitutive models for initially stressed elastic solids from stress and deformation data. A key challenge is that standard data-driven approaches may fail to produce physically consistent models. To address this issue, we develop a mechanics-informed neural network (MINN) which reproduces known stress states in the absence of deformation (i.e., at the identity deformation gradient) and remains consistent across different choices of reference configuration.

3.1. Architecture of the MINN

The architecture of the MINN is illustrated in Fig. 2, where the inputs are the scalar invariants defined in Eq. (7) (in the presence of fibers). The network outputs the scalar strain-energy density W, from which the Cauchy stress tensor is obtained via Eq. (9) using automatic differentiation. To improve generality across constitutive parameter sets within the same class of models, the

constitutive parameters θ are also included as additional inputs to the neural network. For further details on the network architecture, see Appendix A.

The total loss $\mathcal{L}$ minimized by the network consists of two components: a strain-energy density loss $\mathcal{L}_1$ and a Cauchy stress loss $\mathcal{L}_2$. The strain-energy density loss is defined as

$$\mathcal{L}_1 = \left| W\left(\boldsymbol{F}, \boldsymbol{\tau}\right) - W^* \right|_2 , \tag{13}$$

where W^* denotes the target strain energy value. The Cauchy stress loss $\mathcal{L}_2$ is given by

$$\mathcal{L}_2 = \frac{1}{9} \sum_{i=1}^{3} \sum_{j=1}^{3} \left| \sigma_{ij}\left(\boldsymbol{F}, \boldsymbol{\tau}\right) - \sigma_{ij}^* \right|_2 , \tag{14}$$

where σ_{ij} denotes the stress predicted by the neural network, and σ_{ij}^* is the corresponding target stress.

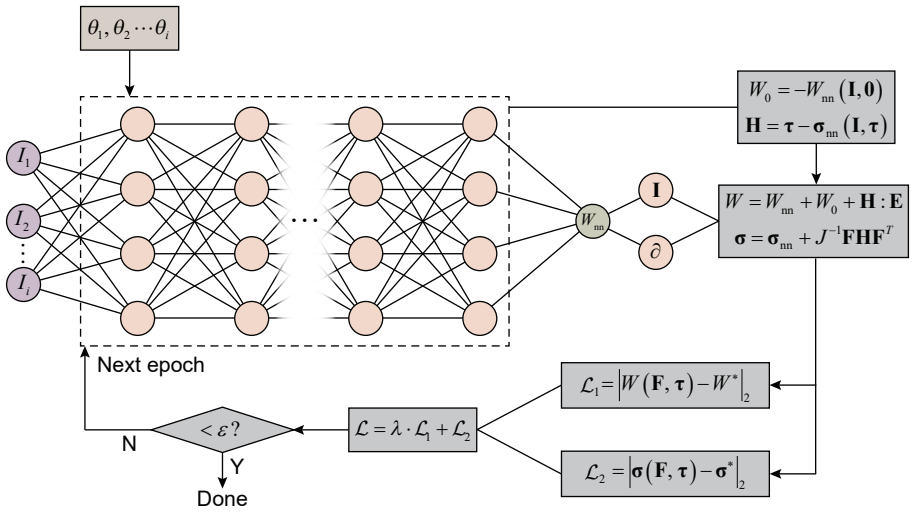


Figure 2: Structure of the proposed MINN framework. The network takes constitutive invariants as inputs and predicts the strain-energy density. During training, the parameters W_0 and $\boldsymbol{H}$ are determined from the ISC conditions. The loss function consists of strain-energy and stress terms, which are jointly minimized during optimization.

To balance the contributions of the two loss components, the total loss function is defined as

$$\mathcal{L} = \lambda \cdot \mathcal{L}_1 + \mathcal{L}_2, \tag{15}$$

where λ is a tunable hyperparameter that determines the relative weight assigned to the strain-energy loss. A sensitivity analysis of λ and the selected value are provided in Appendix A.

We enforce the ISC condition explicitly. In contrast, the ISRI condition is satisfied in an approximate sense via data augmentation, as described in the next section. Following the approach in (Thakolkaran et al., 2022), we express the strain-energy density function in the form

$$W = W_{\mathrm{nn}} + W_0 + \boldsymbol{H} : \boldsymbol{E}, \tag{16}$$

where W_{nn} denotes the strain-energy density predicted by the neural network, W_0 is a scalar correction term, and $\boldsymbol{H} : \boldsymbol{E}$ represents a stress-related correction term. Here, $\boldsymbol{H}$ is a symmetric 3×3 constant matrix, and $\boldsymbol{E} = (\boldsymbol{C} - \mathbf{I})/2$ is the Green–Lagrange strain tensor. The resulting Cauchy stress can be written as

$$\boldsymbol{\sigma} = \boldsymbol{\sigma}_{\mathrm{nn}} + J^{-1}\boldsymbol{F}\boldsymbol{H}\boldsymbol{F}^T,$$

where the stress $\boldsymbol{\sigma}_{\mathrm{nn}}$, corresponding to W_{nn}, is obtained from Eq. (9) via automatic differentiation.

At each training epoch, we enforce that in the absence of deformation, i.e., when the deformation gradient is $\boldsymbol{F} = \mathbf{I}$, the strain-energy density predicted by the neural network corresponds to that of the initially stressed reference configuration, and the predicted Cauchy stress equals the initial stress $\boldsymbol{\tau}$. In other words, the following conditions must be satisfied:

$$(W_{\mathrm{nn}} + W_0 + \boldsymbol{H} : \boldsymbol{E})|_{\boldsymbol{F}=\mathbf{I},\, \boldsymbol{\tau}=\mathbf{0}} = 0, \tag{17}$$

$$\left(\boldsymbol{\sigma}_{\mathrm{nn}} + J^{-1}\boldsymbol{F}\boldsymbol{H}\boldsymbol{F}^T\right)\big|_{\boldsymbol{F}=\mathbf{I}} = \boldsymbol{\tau}. \tag{18}$$

Under these conditions, the initial-stress constitutive model yields zero strain-energy density in the absence of both initial stress and deformation, while the predicted stress in the undeformed configuration recovers the prescribed initial stress (i.e., the ISC condition). Since these constraints must hold at every training epoch, we obtain

$$W_0 = -W_{\mathrm{nn}}(\mathbf{I}, \mathbf{0}), \qquad \boldsymbol{H} = \boldsymbol{\tau} - \boldsymbol{\sigma}_{\mathrm{nn}}(\mathbf{I}, \boldsymbol{\tau}). \tag{19}$$

3.2. Training and testing data

For a given constitutive model, we construct the synthetic training dataset for the MINN by prescribing multiple deformations $\boldsymbol{F}_1$ from a stress-free configuration, thereby generating different initial stresses $\boldsymbol{\tau}$. Subsequently, additional deformations $\boldsymbol{F}$, measured relative to the initially stressed state (see Fig. 1a for a schematic illustration), are prescribed. For each pair $(\boldsymbol{F}, \boldsymbol{\tau})$, we compute the corresponding strain-energy density $W^*(\boldsymbol{F}_2)$ and Cauchy stress $\boldsymbol{\sigma}^*(\boldsymbol{F}_2)$, where $\boldsymbol{F}_2 = \boldsymbol{F}\boldsymbol{F}_1$, which serve as labels for supervised learning. Therefore, each training sample consists of an input–output pair $(\boldsymbol{x}, \boldsymbol{y})$. The input vector $\boldsymbol{x}$ is composed of invariants computed from $\boldsymbol{F}$ and $\boldsymbol{\tau}$, while the output vector $\boldsymbol{y}$ consists of the strain-energy density $W^*(\boldsymbol{F}_2)$ and the Cauchy stress $\boldsymbol{\sigma}^*(\boldsymbol{F}_2)$.

To enforce the ISRI condition in Eq. (10) within the MINN framework, we augment the dataset as follows. For each data point $(\boldsymbol{x}, \boldsymbol{y})$, we fix $\boldsymbol{F}_2 = \boldsymbol{F}\boldsymbol{F}_1$ and generate additional samples that share the same strain-energy density $W^*(\boldsymbol{F}_2)$ and Cauchy stress $\boldsymbol{\sigma}^*(\boldsymbol{F}_2)$, but correspond to different decompositions of $\boldsymbol{F}_2$ through different choices of the initial deformation $\boldsymbol{F}_1$, which in turn induces different values of $\boldsymbol{F}$ and initial stress $\boldsymbol{\tau}$. For each selected $\boldsymbol{F}_1$, the corresponding deformation gradient is given by $\boldsymbol{F} = \boldsymbol{F}_2\boldsymbol{F}_1^{-1}$. This procedure enables efficient generation of a large dataset that satisfies the ISRI condition in Eq. (10).

In total, for the training dataset, random material parameters were selected for each constitutive model, together with 20,000 randomly sampled deformation gradients $\boldsymbol{F}_2$. For each $\boldsymbol{F}_2$, 10 different decompositions into $\boldsymbol{F}$ and $\boldsymbol{F}_1$ were generated to augment the training data and enforce the ISRI condition, resulting in a total of 200,000 augmented samples. Of the resulting data points, 80% are used for training and the remaining 20% for testing (see Appendix A for further details of the dataset construction).

3.3. Training of the MINN for different constitutive models

We first consider the neo-Hookean model as an illustrative example for training the MINN. The corresponding strain-energy density function is

$$W_{\mathrm{nH}}(\boldsymbol{F}_2) = \frac{\mu}{2}\left[\mathrm{tr}(\boldsymbol{F}_2^T\boldsymbol{F}_2) - 3\right], \tag{20}$$

where μ denote the shear moduli, respectively.

Figure 3 presents the training results of the MINN. Figure 3a shows the evolution of the training and validation losses during optimization. Both losses decrease monotonically and converge to

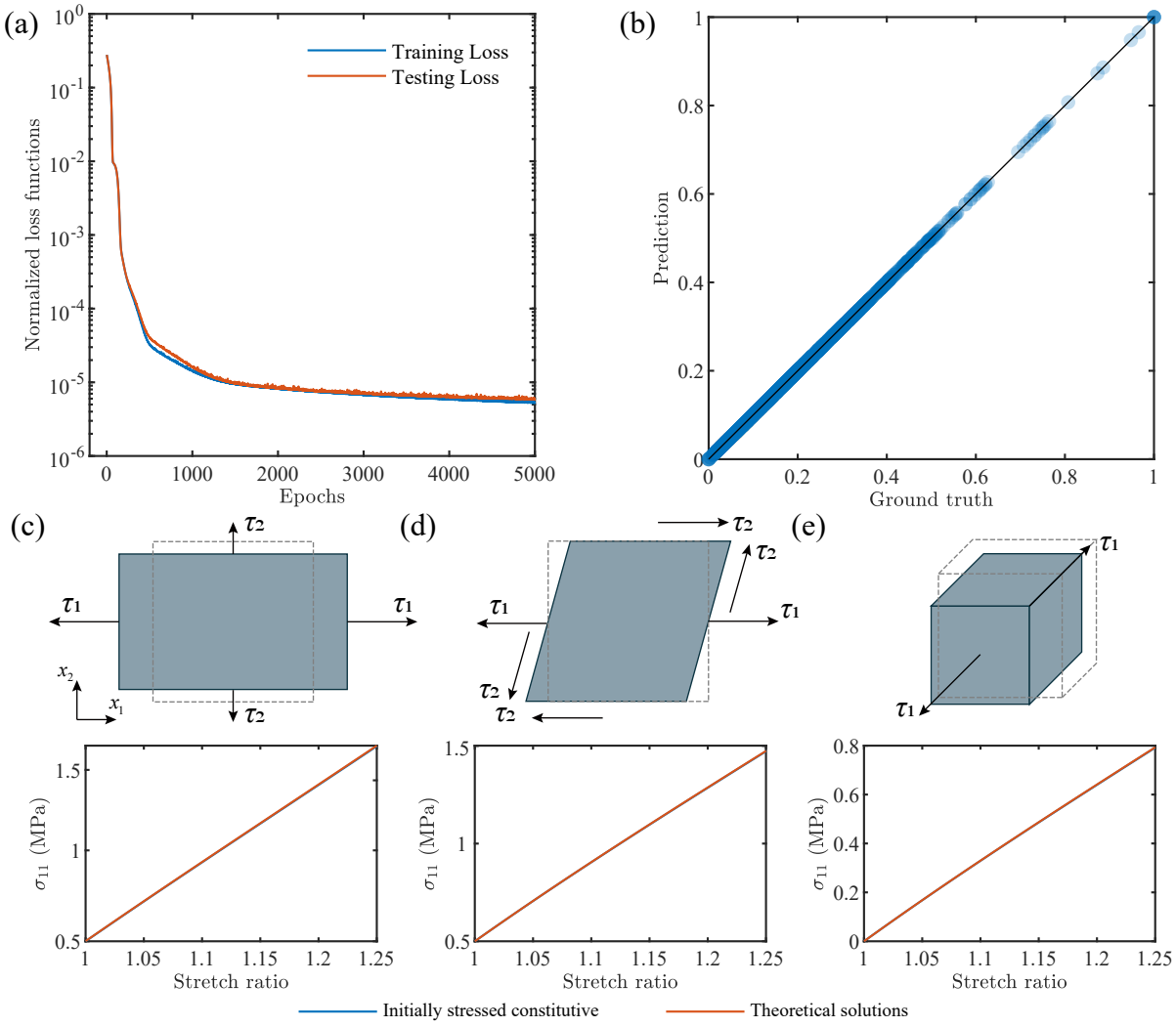


Figure 3: Training performance of the MINN. (a) Evolution of the training and validation losses during optimization. (b) Comparison between the predicted and reference strain-energy values. (c)–(e) Stress–stretch responses predicted by the learned constitutive model and the corresponding theoretical solutions under different initial stress states: (c) in-plane uniaxial stress, (d) in-plane pure shear stress, and (e) out-of-plane uniaxial stress. In all cases, the initial stresses are set to $\tau_1 = 0.5\mu$ and $\tau_2 = 0.3\mu$.

similar values, indicating stable training and good generalization performance. Figure 3b compares the strain-energy predictions of the learned constitutive model with the corresponding reference values for samples spanning a wide range of initial stress states and deformation gradients in the testing dataset, demonstrating excellent agreement.

To further assess the ability of the MINN to capture the constitutive behavior of initially stressed materials, we compare the stress–stretch responses predicted by the learned constitutive model with the corresponding theoretical solutions under different initial stress states, including in-plane uniaxial stress, in-plane pure shear stress, and out-of-plane stress, as shown in Figs. 3c–e. In all cases, the initial stresses are set to $\tau_1 = 0.5\mu$ and $\tau_2 = 0.3\mu$. Excellent agreement is observed between the predicted and theoretical responses, demonstrating that the MINN accurately reproduces the mechanical response associated with a wide range of initial stress states.

We also consider a case in which the strain-energy data $W^*(\boldsymbol{F}_2)$ are unavailable. This is achieved

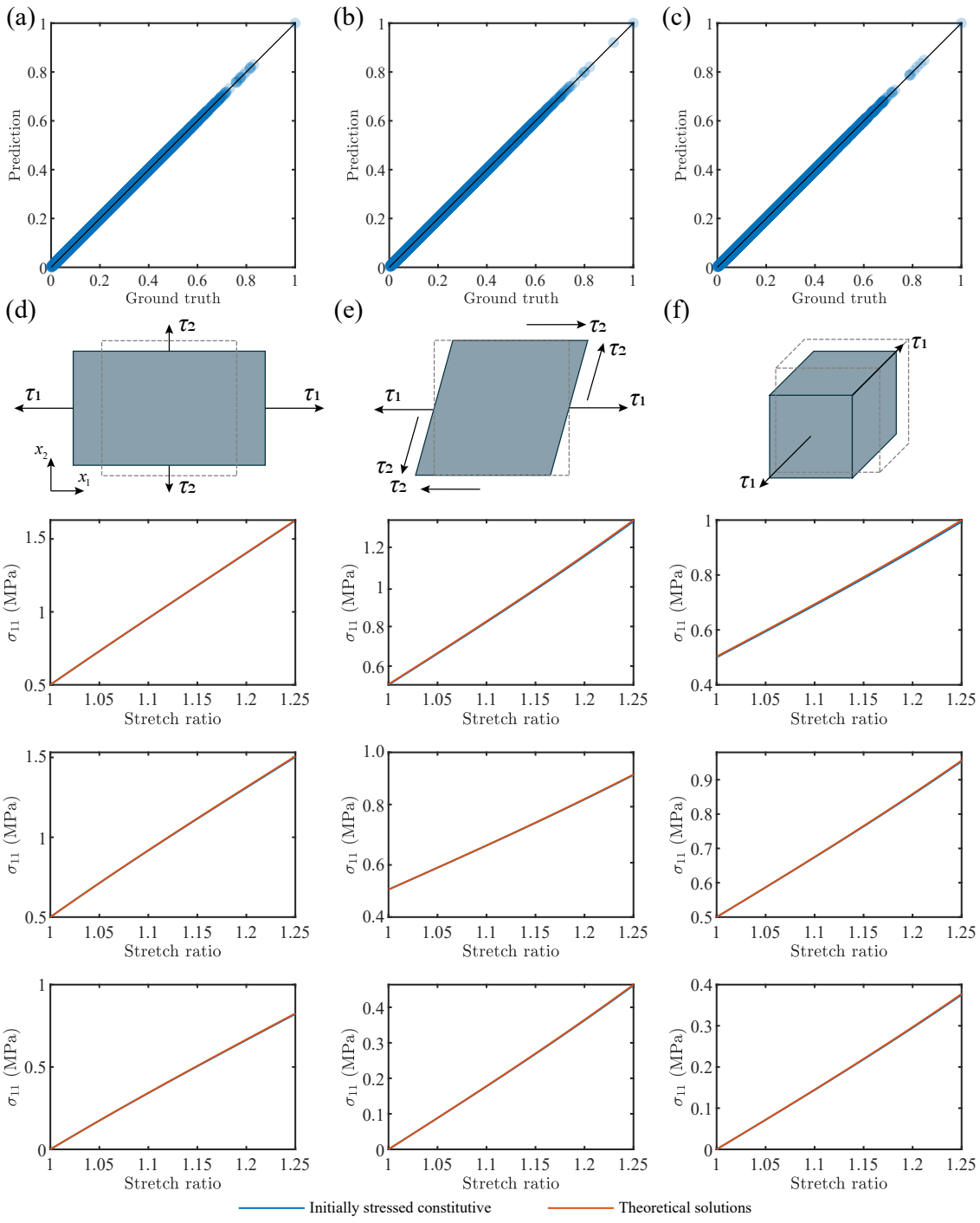


Figure 4: Training and validation results of the MINN for different constitutive models: (a,d) Mooney–Rivlin model, (b,e) Arruda–Boyce model, and (c,f) Gent model. Panels (a)–(c) show the predicted and reference strain–energy values, while panels (d)–(f) compare the stress–stretch responses predicted by the learned constitutive models with the corresponding reference solutions.

by setting $\lambda = 0$ in Eq. (15), so that the network is trained solely using stress data. The resulting predictions are nearly indistinguishable from those obtained when both stress and strain-energy labels are included (Appendix B), for the constitutive models considered here. This observation is

consistent with the fact that the stress tensor is directly related to the strain-energy function through differentiation, such that sufficiently rich stress measurements strongly constrain the underlying constitutive response.

In particular, if the complete and exact stress field is known over a connected deformation domain, the strain-energy function can, in principle, be recovered from the stress field up to a function $g(\boldsymbol{\tau})$ that is independent of deformation by integrating the stress with respect to the deformation gradient. Consequently, for sufficiently smooth constitutive responses and sufficiently rich sampling of the deformation domain, explicit strain-energy labels are not expected to provide substantial additional independent information for determining the stress response. For an unknown constitutive law, however, stress data alone do not generally determine the absolute value of the strain-energy density uniquely, and the strain-energy function learned from stress data may therefore differ from the true strain-energy function by $g(\boldsymbol{\tau})$. This ambiguity does not affect the constitutive response, since the stress and its first derivative with respect to the deformation are determined by the first and second derivatives of the strain-energy function, respectively. Thus, while strain-energy labels can help fix the otherwise undetermined energy reference $g(\boldsymbol{\tau})$, they are not essential for recovering the stress response and its first-order variation, provided that the available stress–deformation data sufficiently constrain the relevant deformation domain.

Finally, the proposed MINN was further applied to several constitutive models exhibiting stronger nonlinear stiffening, including the Mooney–Rivlin, Arruda–Boyce, and Gent models. The corresponding training histories and predictive performance of the learned constitutive models are presented in Fig. 4. The results demonstrate that the proposed framework accurately captures a broad range of constitutive behaviors, including materials with pronounced strain-hardening effects.

4. Finite element implementation of the initially stressed constitutive model

4.1. Implementation of the constitutive model

To enable the proposed constitutive model to be used in numerical simulations, we develop a user-defined material subroutine that can be incorporated into general nonlinear finite element analysis (FEA). As a demonstration, we implement the framework in the commercial FEA software ABAQUS (Dassault Systèmes Simulia Corp., 2021).

Following training, the neural network is exported in TorchScript format, a serialized representation of the PyTorch model that enables efficient deployment in production environments (PyTorch Team, 2024). A C++ dynamic link library (DLL) is then developed to provide an interface between the trained neural network and the UMAT subroutine in ABAQUS (Dassault Systèmes Simulia Corp., 2021).

The C++ library encapsulates the neural network and provides the first- and second-order derivatives of the strain-energy density with respect to the invariants. These derivatives are required for evaluating both the stress tensor and the consistent material tangent stiffness matrix used in the finite element formulation. Further details of the implementation are provided in Appendix C.

Through this framework, the MINN-based constitutive model for initially stressed solids can be efficiently incorporated into general nonlinear finite element simulations. In the following sections, we demonstrate the effectiveness of the proposed approach using two representative benchmark problems.

4.2. Small-on-large: small-amplitude waves on initially stressed solids

For the long-term goal of personalized medicine, constitutive models must ultimately be calibrated to the mechanical properties of individual tissues. Small-amplitude elastic waves, including

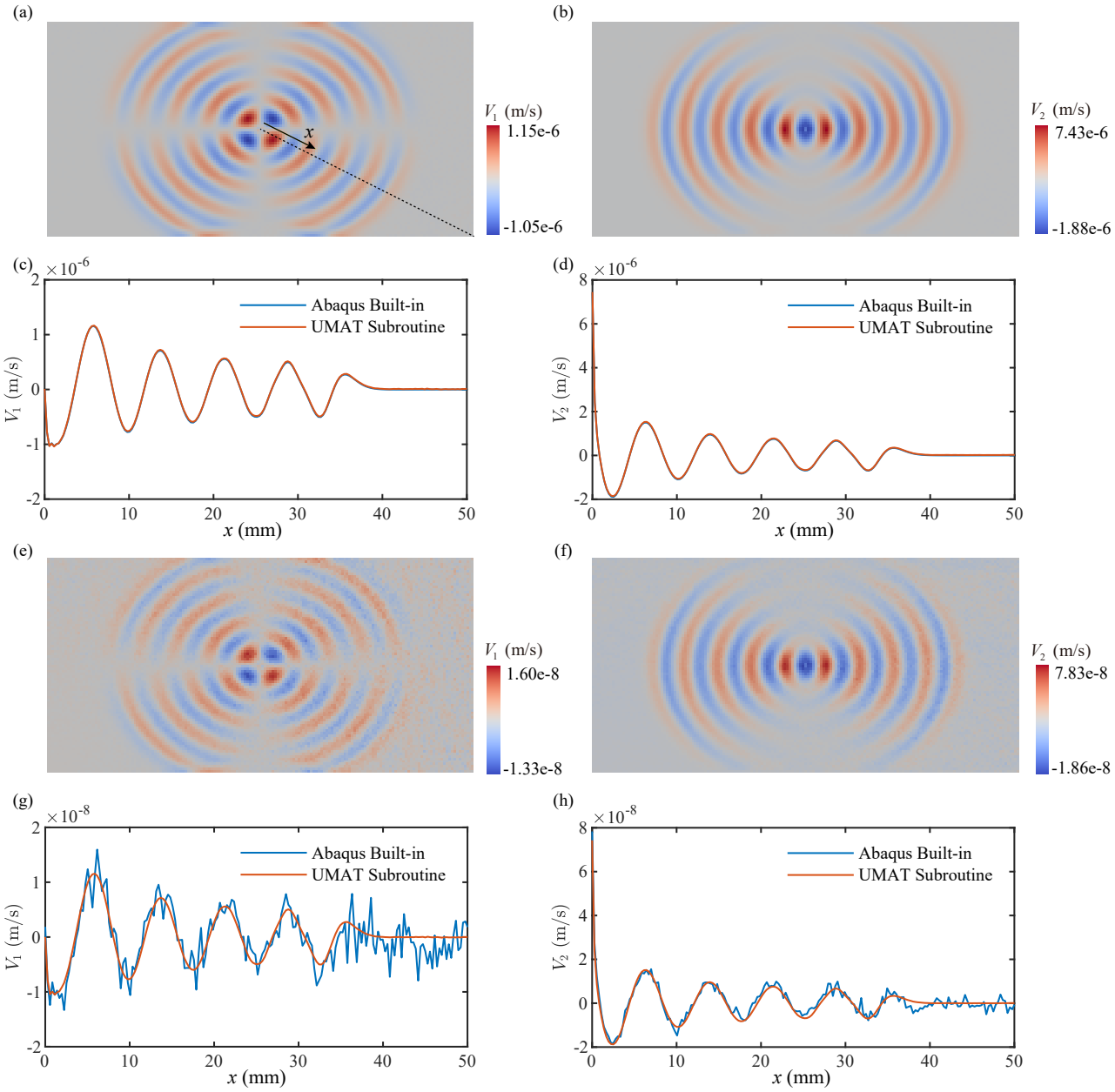


Figure 5: Comparison between the conventional finite element analysis and the proposed initially stressed constitutive model. (a,b) Wavefield snapshots predicted by the ABAQUS built-in model under a large-amplitude perturbation. (c,d) Comparison of the wave profiles predicted by the ABAQUS built-in model and the initially stressed constitutive model for the large-amplitude perturbation. (e,f) Wavefield snapshots predicted by the ABAQUS built-in model under a small-amplitude perturbation. (g,h) Comparison of the wave profiles predicted by the ABAQUS built-in model and the initially stressed constitutive model for the small-amplitude perturbation.

guided waves and ultrasound waves, provide a promising means of probing tissue mechanics non-invasively and estimating the underlying strain-energy density function. For this reason, we first demonstrate the effectiveness of the proposed MINN framework for modeling linear elastic wave propagation in initially stressed solids.

The propagation of elastic waves is highly sensitive to initial stress through the acoustoelastic

effect. Since the deformation associated with wave motion is typically much smaller than the deformation required to generate the initial stress, such problems are commonly referred to as *small-on-large* problems. The acoustoelastic effect not only enables the manipulation of wave propagation through prestress but also provides a powerful mechanism for inferring stress states from wave measurements. Consequently, acoustoelasticity has attracted renewed attention in recent years.

A challenge in simulating small-on-large problems is that the conventional approach requires first applying a large deformation to generate the initial stress and then superimposing a much smaller perturbation. When the perturbation amplitude becomes sufficiently small, significant round-off errors may arise due to the subtraction of quantities with vastly different magnitudes. In contrast, these numerical difficulties are avoided when using an initially stressed constitutive model.

To demonstrate this advantage, we study shear-wave propagation in a neo-Hookean material subjected to uniaxial prestress of 0.5μ along the horizontal direction, corresponding to a displacement of $U_1 = 32.6$ mm for our model. Plane waves are then generated by prescribing the vibration amplitude (denoted by u_2) of the center along the vertical direction. Consistent with acoustoelastic theory, the wavefronts no longer remain circular but instead become elliptical, as shown in Figs. 5(a), (b), (e), and (f). Figures 5(c) and (d) show that when the perturbation amplitude is relatively large ($u_2 = 10^{-7}U_1$), the conventional ABAQUS approach and the initially stressed constitutive model produce nearly identical results. However, as the perturbation amplitude decreases, the conventional approach becomes increasingly susceptible to numerical round-off errors. For a perturbation amplitude of $u_2 = 10^{-9}U_1$, which is relevant to many ultrasonic and elastographic applications, substantial numerical artifacts are observed in the conventional simulation. In contrast, the initially stressed constitutive model remains accurate and stable, as demonstrated in Figs. 5(g) and (h).

4.3. Large-on-large: corneal removal for vision correction

When finite deformations are superimposed on an initially stressed reference configuration, the resulting problem is referred to as a large-on-large problem. Here, we present a representative example: predicting the deformation of the cornea after surgical ablation. The cornea is initially stressed by intraocular pressure (IOP) in vivo. Upon laser ablation, the cornea is further deformed by the IOP and reaches a new configuration, which is intended to correctly focus light on the retina for vision correction. In practical cases, only the geometry of the deformed cornea under IOP can be measured. Therefore, constitutive models that account for initial stress are valuable for surgical planning.

To construct an initially stressed constitutive model for the cornea, we adopt the Holzapfel–Gasser–Ogden (HGO) model (Holzapfel and Ogden, 2003; Li et al., 2024):

$$W = \frac{\mu}{2}\left(I_1 - 3\right) + \frac{k_1}{k_2}\left\{e^{k_2[\kappa(I_1-3)+(1-3\kappa)(I_4-1)]^2} - 1\right\}, \tag{21}$$

where the additional terms model the nonlinear elastic response of the collagen fibers in the strain-energy function. Here, k_1 characterizes the anisotropic tensile response, k_2 accounts for the nonlinear stiffening of collagen fibers under large deformations, and κ denotes the fiber dispersion parameter. Specifically, $\kappa = 0$ corresponds to unidirectionally aligned fibers, while $\kappa = 1/3$ represents an isotropic distribution of fibers. Pandolfi and Holzapfel (Pandolfi, 2020; Pandolfi and Holzapfel, 2008) showed that the collagen fibrils in the central cornea are approximately organized along two orthogonal directions, with relatively small dispersion parameters ($\kappa < 0.13$). In the axisymmetric formulation adopted here, this three-dimensional fiber architecture is approximated by a single circumferential fiber direction, $\kappa = 0$. The collagen fibril direction is specified in the initially

stressed reference configuration as $\boldsymbol{M} = (1, 0, 0)^T$, and its direction, and magnitude, in the current configuration evolves with the deformation $\boldsymbol{FM}$. See Mukherjee et al. (2022) for details.

To construct an initially stressed version of the HGO model, we employ the proposed MINN framework and increase the number of neurons in each hidden layer to 1000 to accommodate the increased complexity associated with anisotropy. Training data are generated from the HGO model, and the trained network is subsequently implemented in ABAQUS through a UMAT subroutine for finite element simulations.

We then construct a finite element model of the cornea. For simplicity, an axisymmetric geometry is adopted, with collagen fibers assumed to be oriented in the circumferential direction. The above assumptions introduce a simplification relative to the actual three-dimensional collagen architecture of the cornea. In particular, the neglected orthogonal fiber family, finite fiber dispersion, and spatial variation of fiber orientation may affect the anisotropic stiffness and therefore contribute to discrepancies between the modeled and actual mechanical responses. The material parameters and mechanical responses obtained from the present model should therefore be interpreted as effective quantities within the adopted axisymmetric representation, rather than as a complete characterization of the intrinsic three-dimensional anisotropic properties of the cornea. An intraocular pressure (IOP) is applied uniformly normal to the inner corneal surface. The inner radius and wall thickness are set to 7 mm and 0.5 mm, respectively. Importantly, these geometric parameters correspond to the initially stressed configuration $\mathcal{B}_1$. In the absence of an initial stress field, the same geometry would not be in equilibrium under the applied IOP and would therefore undergo further deformation. Consequently, the corresponding initial stress field must be incorporated into the constitutive model to maintain the prescribed geometry.

In clinical practice, the IOP is routinely measured and readily available (Yan et al., 2026). To estimate the initial stress field associated with the measured geometry, we construct an auxiliary finite element model with the same geometry as the cornea. An auxiliary shear modulus of 50 MPa is assigned to this model, selected based on a convergence analysis using auxiliary shear moduli of 20, 50, and 100 MPa. The resulting maximum circumferential stresses are 21.80, 21.81, and 21.81 kPa, respectively, indicating that the recovered initial stress field has essentially converged at 50 MPa. In addition, the deformation produced by the applied IOP is negligible, with an apical displacement of only 0.562 μm, allowing the measured geometry to be treated as effectively undeformed while the corresponding equilibrium stress field is computed. The resulting stress field is then imported as the initial stress $\boldsymbol{\tau}$ in the initially stressed constitutive model.

Figure 6 presents the corneal stress and deformation fields predicted using conventional and initial stress-based modeling approaches. Figure 6a shows the circumferential stress distribution obtained by applying intraocular pressure to the stress-free configuration, while Fig. 6b presents the circumferential stress distribution after incorporating the prestress field through the initial stressed constitutive model. Figures 6c and d compare the radial deformation distributions following corneal ablation. Figure 6c corresponds to the model generated by applying intraocular pressure to the stress-free configuration, whereas Figure 6d shows the deformation predicted using the initial stressed constitutive model.

For quantitative comparison, the stress and radial-displacement distributions along the outer corneal surface extracted from Figs. 6a and b, and Figs. 6c and d, are shown in Figs. 6e and f, respectively. For clarity, only one half of the cornea, extending from the apex to the periphery, is presented. The initial stress predicted by the proposed approach exhibits slight deviations from the reference solution obtained using the conventional finite element procedure. These differences arise from the approximation used to estimate the initial stress field directly from the measured geometry and IOP. Despite these discrepancies, the resulting deformation after corneal ablation is predicted with high accuracy. In particular, the error in the radial displacement at the corneal

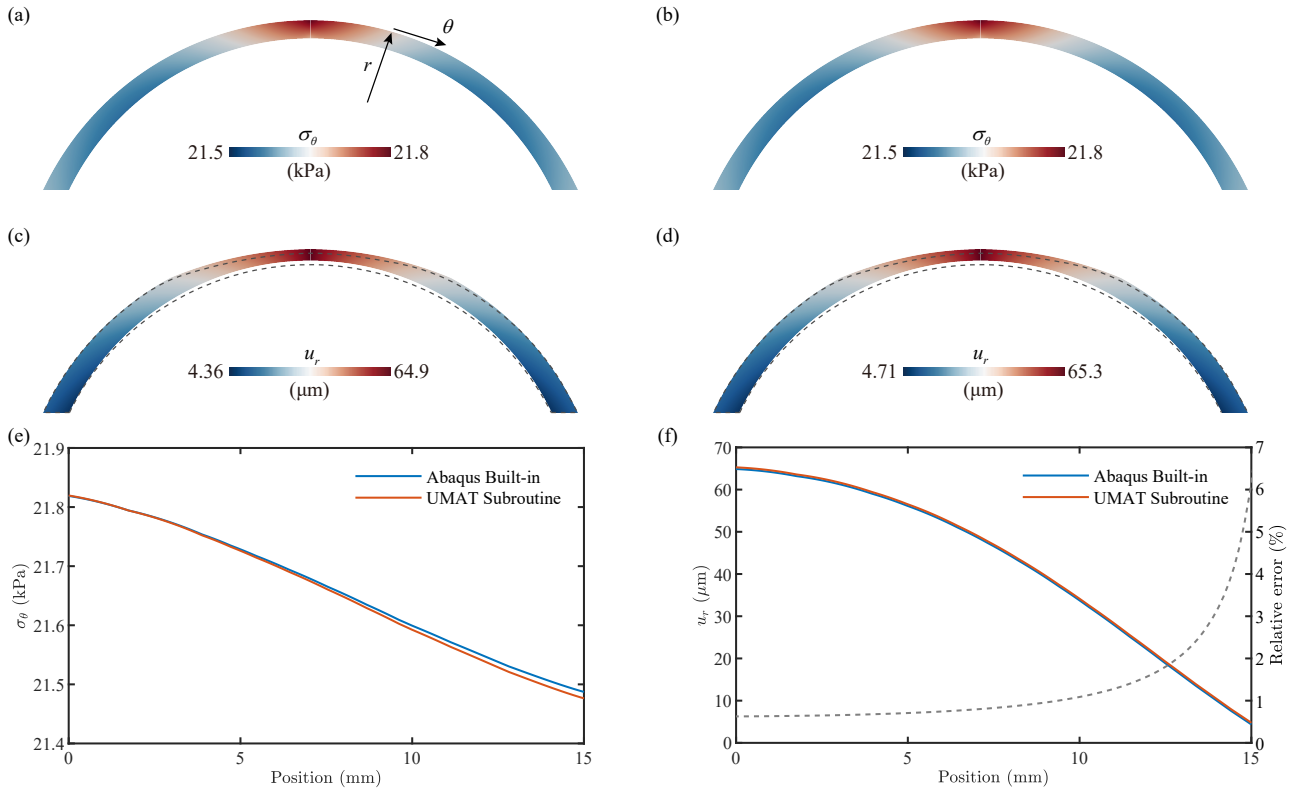


Figure 6: Corneal prestress and post-ablation deformation predicted using the initially stressed constitutive model. (a) Circumferential stress distribution obtained by applying intraocular pressure (IOP) to the stress-free configuration. (b) Circumferential stress distribution in the cornea after incorporating the estimated prestress field into the initially stressed model. (c) Radial deformation following corneal ablation predicted by the conventional finite element approach. (d) Radial deformation following corneal ablation predicted by the initially stressed constitutive model. (e) Circumferential prestress σ_θ along the outer corneal surface from the apex to the periphery. (f) Radial displacement u_r along the outer corneal surface after corneal ablation.

apex, which is the quantity most relevant to vision correction, is 0.39 μm, corresponding to less than 1% of its magnitude. These results demonstrate that the proposed framework can accurately predict the mechanical response of the cornea following tissue removal and highlight its potential for subject-specific surgical planning.

5. Experimental verification of the initially stressed constitutive modeling by optical coherence elastography

To experimentally validate the proposed constitutive modeling framework, we performed a proof-of-concept study using a corneal phantom designed to mimic the in vivo cornea under intraocular pressure (IOP). The objective was to assess whether constitutive parameters identified directly from an initially stressed configuration could be used to predict subsequent mechanical responses under altered loading conditions, without reconstructing a stress-free reference state. Optical coherence elastography (OCE), a technique developed for non-invasive characterization of corneal biomechanics, was employed to identify the constitutive parameters of the phantom. Specifically, guided-wave measurements were used to estimate the material parameters independent of the initial stress. These parameters were then incorporated into the initially stressed constitutive model to predict the deformation of the phantom under different prestress states. By comparing the predicted and measured

deformations, we evaluate the ability of the proposed framework to characterize and predict the mechanical response of prestressed soft materials.

5.1. OCE measurements on the corneal phantom

The corneal phantom consisted of a curved PDMS membrane with an initial radius of curvature of 8.4 mm and a thickness of 0.55 mm. The phantom was mounted onto a water-filled chamber connected to a water column, allowing the internal pressure to be controlled. The applied pressure generated an initial stress field within the phantom and brought it to the initially stressed configuration $\mathcal{B}_1$.

Experiments were performed using a custom-built swept-source optical coherence tomography (OCT) system (Fig. 7a) operating at a central wavelength of 1310 nm and an A-line rate of 100 kHz. The geometry of the phantom in the initially stressed configuration, including the radius of curvature and wall thickness, was measured directly from OCT images. OCE measurements were then performed by exciting guided waves over the frequency range of 2–16 kHz (Fig. 7b), generating predominantly the symmetric (S_0) and antisymmetric (A_0) Lamb-wave modes.

Under the applied pressure ($\uparrow$), the phantom deformed to an anterior-surface radius of curvature of 7.64 mm and a central thickness of 0.425 mm. Wave-induced displacements were extracted from the OCT phase measurements and transformed into the frequency domain to obtain the harmonic wave fields (Fig. 7d). For each excitation frequency, the surface displacement profile (Fig. 7c) was further transformed into the wavenumber domain. The dominant spectral peaks corresponding to the A_0 and S_0 modes were identified, and the phase velocities were calculated from $v = 2\pi f/k$, where k denotes the corresponding wavenumber. The experimentally measured dispersion curves are shown as blue markers in Fig. 7e.

5.2. Characterization of constitutive parameters from OCE data

To interpret the OCE measurements, we adopted the initially stressed neo-Hookean constitutive model and treated the shear modulus as an unknown material parameter. As discussed in Section 4.3, the prestress field in the phantom was estimated from the applied water pressure using an auxiliary finite element model. Based on the measured geometry of the prestressed configuration $\mathcal{B}_1$ and the estimated prestress field, numerical simulations were performed using the initially stressed constitutive model. The shear modulus was then identified by fitting the predicted dispersion curves to the experimentally measured A_0 and S_0 phase velocities. The best-fit dispersion curves are shown by the solid blue lines in Fig. 7e, yielding a shear modulus of 44.16 kPa, in good agreement with the value obtained from independent tensile tests (see Appendix D for data and the comparison).

5.3. Deformations of the phantom from the initially stressed configuration

Having identified the constitutive parameters, we next evaluate whether the initially stressed constitutive model can accurately predict subsequent deformations relative to the initially stressed configuration $\mathcal{B}_1$. To this end, the internal pressure was reduced, and both the geometry and Lamb-wave dispersion of the phantom were measured again. The identified constitutive model was then used to predict the new equilibrium configuration without further parameter adjustment.

Under the reduced pressure ($\downarrow$), the experimentally measured radius of curvature and central thickness were 8.15 mm and 0.544 mm, respectively, while the finite element model predicted values of 8.19 mm and 0.546 mm. Both the thickness and the surface curvature were in close agreement between simulation and experiment, as shown in Fig. 7f, where the dashed lines denote the predictions obtained using the initially stressed constitutive model.

To further validate the model, Lamb-wave measurements were repeated under the reduced-pressure condition. The experimentally measured dispersion relations are shown by the red markers

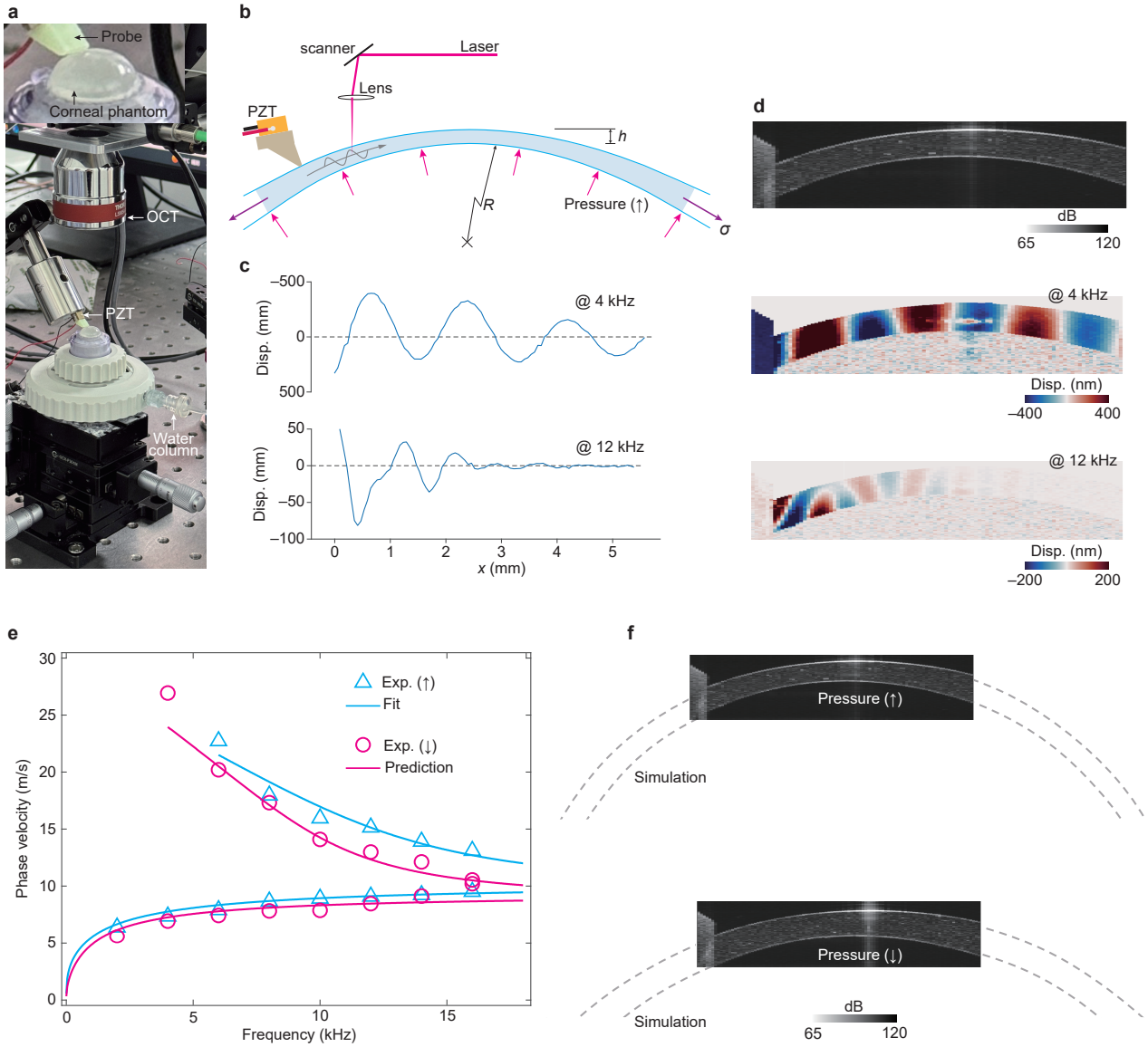


Figure 7: Experimental validation of the initially stressed constitutive model. (a) Photograph of the experimental setup, showing the OCT system and the PZT-driven probe used for wave excitation. (b) Schematic of the corneal phantom and the corresponding initial stress field. (c) Surface displacement profiles extracted from the outer surface of the phantom at 4 kHz and 12 kHz under high IOP (IOP $\approx$ 7.26 kPa). The distance x is measured from the excitation point. (d) Real parts of the full wave fields corresponding to the displacement profiles shown in (c). (e) Dispersion relations of the A0 and S0 modes measured at high (↑) and low (↓) IOPs. (f) Comparison of corneal phantom deformations between experiments and simulations under different IOPs. The dashed lines denote the phantom shapes predicted by the initially stressed constitutive model.

in Fig. 7e and exhibit excellent agreement with the finite element predictions. The ability to simultaneously predict both the deformed geometry and the guided-wave dispersion demonstrates that the identified constitutive model accurately captures the mechanical response of the phantom under changing prestress conditions.

These experiments highlight an important feature of the proposed framework. In this experiment, the neural network learns the constitutive response and identifies the material parameters within the prescribed initially stressed neo-Hookean model, rather than discovering the constitutive

form itself. All measurements, constitutive parameter identification, and model validation were performed directly on the loaded configuration of the phantom. No reconstruction of a stress-free reference state was required. Instead, the initial stress field was treated as an explicit constitutive variable and incorporated into the constitutive model through the proposed MINN framework. This capability is particularly attractive for biological tissues, where stress-free configurations are generally inaccessible *in vivo*. More broadly, the combination of stress characterization, constitutive learning, and predictive mechanical simulation provides a potential route toward patient-specific biomechanical modeling and surgical planning.

6. Learning Both the Stress Field and Constitutive Model

Recent studies have demonstrated the potential of neural-network-based constitutive modeling through unsupervised learning approaches (Flaschel et al., 2021; Liu et al., 2025; Thakolkaran et al., 2022; Wu et al., 2025). In these frameworks, the training data consist only of displacement fields and reaction forces, thereby avoiding the need for direct stress measurements. This feature is attractive because internal stresses are often inaccessible experimentally. The present framework differs fundamentally in that the initial stress enters explicitly as a constitutive variable. Consequently, reliable measurements of the internal stress field become an essential requirement.

To address this challenge, we recently developed Acoustoelastic Imaging (AEI), a non-destructive imaging technique that reconstructs internal stress fields from shear-wave measurements (Duan et al., 2026). AEI is able to reconstruct both stress magnitudes and principal stress directions. Importantly, this reconstruction does not require prior knowledge of the constitutive model. As a result, AEI provides a natural experimental companion to the constitutive modeling framework proposed here.

To demonstrate this integration, we consider a heterogeneous reference stress field in a neo-Hookean material generated through local thermal expansion. This stress field is then reconstructed using AEI. Figure 8a shows the reconstructed in-plane normal and shear stresses. The reconstructed stress field is subsequently incorporated into the previously learned initially stressed neo-Hookean model, $W_{\mathrm{nH}}(\boldsymbol{F}, \boldsymbol{\tau})$, as the initial stress field $\boldsymbol{\tau}$.

We next investigate the effect of the reconstructed initial stress on the subsequent mechanical response of the material. Uniaxial loading is applied to the prestressed specimen, and the resulting mechanical responses are compared with predictions obtained by neglecting the initial stress, i.e., using $W(\boldsymbol{F}, \boldsymbol{0})$. We find that both the strain field and the overall stress–strain response are significantly affected by the initial stress $\boldsymbol{\tau}$, as shown in Figs. 8b and c. To visualize this effect, strain fields at overall strains of 0.02, 0.04, and 0.06 are presented. The results indicate that incorporating the initial stress produces a markedly heterogeneous strain field.

Finally, the predictions from the learned constitutive model $W(\boldsymbol{F}, \boldsymbol{\tau})$ are compared with the reference solution after uniaxial loading. The close agreement observed in Figs. 8d and e demonstrates that the proposed framework, combined with AEI, can accurately predict the mechanical response of heterogeneous initially stressed materials.

Unlike conventional data-driven constitutive modeling, where stress is treated as an output quantity inferred from displacement and force measurements, the present framework treats the initial stress itself as a constitutive variable. Consequently, stress is no longer merely a training label but becomes part of the constitutive description. This distinction fundamentally changes the requirements for constitutive learning and motivates the integration of stress-imaging techniques such as AEI. More broadly, the proposed framework suggests a shift from constitutive modeling based solely on kinematic measurements toward constitutive modeling informed by both deformation

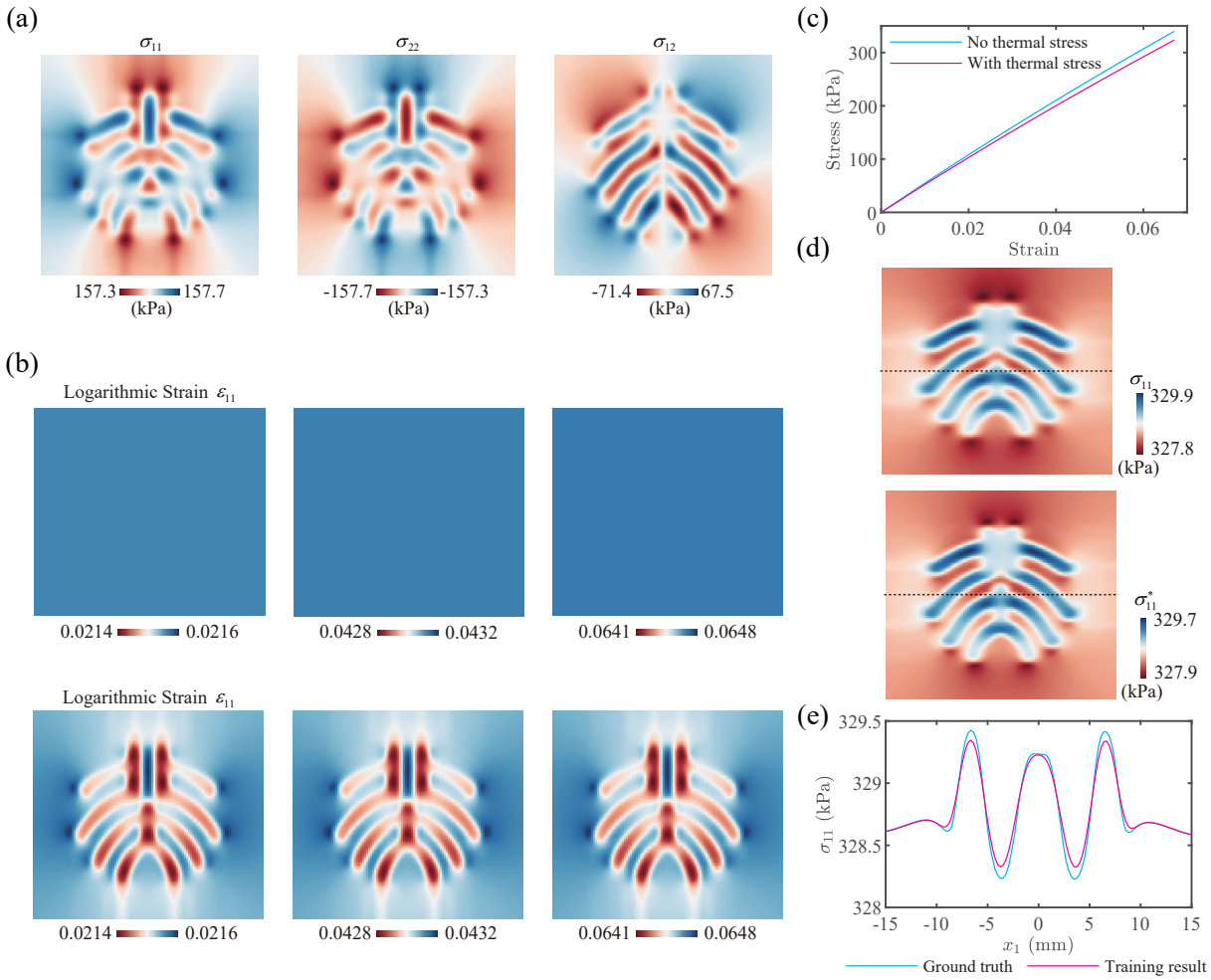


Figure 8: Integration of Acoustoelastic Imaging (AEI) and mechanics-informed constitutive modeling. (a) In-plane normal and shear stresses reconstructed by AEI, where the reference stress field is generated through local thermal expansion. (b) Strain-field evolution during uniaxial loading with and without incorporation of the reconstructed initial stress. (c) Comparison of the uniaxial stress–strain responses obtained with and without consideration of the initial stress. (d) Comparison between the stress field predicted by the learned initially stressed constitutive model and the reference solution after uniaxial loading. (e) Horizontal stress profile extracted from panel (d).

and mechanical state, which may be particularly valuable for biological tissues where residual and physiological stresses play an important role in mechanical function.

The present study represents an initial step toward constitutive modeling directly from loaded configurations. Future developments may incorporate fully three-dimensional stress reconstruction, more complex anisotropic constitutive behaviors, and experimental measurements in biological tissues. Such advances would further strengthen the connection between stress imaging, constitutive characterization, and predictive mechanical simulation.

7. Conclusion

We have developed a mechanics-informed neural network (MINN) framework for constructing constitutive models of initially stressed elastic solids directly from stress and deformation data, without requiring reconstruction of a stress-free reference configuration. The framework explicitly

incorporates the initial stress as a constitutive variable and enforces the key physical constraints associated with initially stressed elasticity, including initial stress compatibility and initial stress reference independence.

The proposed MINN was used to construct initially stressed versions of several hyperelastic constitutive models, including the Mooney–Rivlin, Arruda–Boyce, Gent, and Holzapfel–Gasser–Ogden models. The learned constitutive models were implemented in ABAQUS through a UMAT subroutine and validated in both small-on-large and large-on-large deformation problems. Accurate predictions were obtained for wave propagation in prestressed solids and for corneal deformation following surgical ablation.

Finally, we demonstrated the integration of the proposed framework with Acoustoelastic Imaging (AEI), which provides the stress information required for constitutive modeling of initially stressed materials. Together, these developments establish a framework for constitutive modeling directly from stress data and provide a pathway toward subject-specific mechanical modeling of soft materials and biological tissues in their natural loaded state.

Declaration of Competing Interest

The authors declare that they have no known competing financial interests or personal relationships that could have appeared to influence the work reported in this paper.

Acknowledgement

This work is supported by the National Natural Science Foundation of China (Grant Nos. 12532016 and 12472176), the Beijing Natural Science Foundation (Grant No. F262034), and the Fundamental Research Funds for the Central Universities, Peking University.

References

Agosti, A., Gower, A.L., Ciarletta, P., 2018. The constitutive relations of initially stressed incompressible Mooney–Rivlin materials. Mech. Res. Commun. 93, 4–10.

Brodnik, N.R., Muir, C., Tulshibagwale, N., Rossin, J., Echlin, M.P., Hamel, C.M., Kramer, S.L.B., Pollock, T.M., Kiser, J.D., Smith, C., Daly, S.H., 2023. Perspective: Machine learning in experimental solid mechanics. J. Mech. Phys. Solids 173, 105231. doi:10.1016/j.jmps.2023.105231.

Chester, S.A., Anand, L., 2011. A thermo-mechanically coupled theory for fluid permeation in elastomeric materials: Application to thermally responsive gels. J. Mech. Phys. Solids 59, 1978–2006. doi:10.1016/j.jmps.2011.07.005.

Chuong, C.J., Fung, Y.C., 1986. On residual stresses in arteries. J. Biomech. Eng. 108, 189–192.

Ciarletta, P., Destrade, M., Gower, A.L., Taffetani, M., 2016. Morphology of residually stressed tubular tissues: Beyond the elastic multiplicative decomposition. J. Mech. Phys. Solids 90, 242–253. doi:10.1016/j.jmps.2016.02.020.

Dassault Systèmes Simulia Corp., 2021. Abaqus 2021 Documentation. Dassault Systèmes Simulia Corp.. Providence, RI, USA.

Dorfmann, L., Ogden, R.W., 2021. The effect of residual stress on the stability of a circular cylindrical tube. J. Eng. Math. 127, 9. doi:10.1007/s10665-021-10097-4.

Du, Y., Lü, C., Chen, W., Destrade, M., 2018. Modified multiplicative decomposition model for tissue growth: Beyond the initial stress-free state. J. Mech. Phys. Solids 118, 133–151. doi:10.1016/j.jmps.2018.05.014.

Du, Y.K., Lü, C.F., Destrade, M., Chen, W.Q., 2019. Influence of initial residual stress on growth and pattern creation for a layered aorta. Sci. Rep. 9, 1–9. doi:10.1038/s41598-019-44694-2.

Duan, Y., Destrade, M., Tan, W., Li, G.Y., 2026. Direct stress imaging from shear wave propagation. arXiv arXiv:2606.25385. URL: https://arxiv.org/abs/2606.25385.

Flaschel, M., Kumar, S., De Lorenzis, L., 2021. Unsupervised discovery of interpretable hyperelastic constitutive laws. Comput. Methods Appl. Mech. Eng. 381, 113852.

Fung, Y.C., 1990. Biomechanics: Motion, Flow, Stress and Growth. Springer-Verlag, New York.

Fung, Y.C., 1991. What are the residual stresses doing in our blood vessels? Ann. Biomed. Eng. 19, 237–249. doi:10.1007/BF02584301.

Gower, A.L., Ciarletta, P., Destrade, M., 2015. Initial stress symmetry and its applications in elasticity. Proc. R. Soc. A 471, 20150448.

Gower, A.L., Shearer, T., Ciarletta, P., 2017. A new restriction for initially stressed elastic solids. Q. J. Mech. Appl. Math. 70, 455–478.

Gower, A.L., Shearer, T., Ciarletta, P., Destrade, M., 2025. The elastic stored energy of initially strained, or stressed, materials: restrictions and third-order expansions. Proceedings of the Royal Society A: Mathematical, Physical and Engineering Sciences 481. doi:10.1098/rspa.2024.0272.

Hoger, A., 1986. On the determination of residual stress in an elastic body. J. Elast. 16, 303–324.

Hoger, A., 1996. Compatibility and the genesis of residual stress by volumetric growth. J. Math. Biol. 34, 889–914.

Holzapfel, G.A., Ogden, R.W., 2003. Biomechanics of Soft Tissue in Cardiovascular Systems. volume 441 of *CISM Courses and Lectures*. Springer, Vienna.

Johnson, B.E., Hoger, A., 1995. The use of a virtual configuration in formulating constitutive equations for residually stressed elastic materials. J. Elast. 41, 177–215. doi:10.1007/BF00041874.

Kang, W., Li, L., Song, H., Li, Y., Zhang, M., Wang, L., Fan, Y., 2025. Advances and challenges in the mechanics of biological soft tissues: Test methods, modeling, and applications. Acta Mech. Sin. 41, 624409. doi:10.1007/s10409-024-62409-x.

Klein, D.K., Fernández, M., Martin, R.J., Neff, P., Weeger, O., 2022. Polyconvex anisotropic hyperelasticity with neural networks. J. Mech. Phys. Solids 159, 104703.

Li, G.Y., Feng, X., Yun, S.H., 2024. Simultaneous tensile and shear measurement of the human cornea in vivo using S0- and A0-wave optical coherence elastography. Acta Biomater. 175, 114–122. doi:10.1016/j.actbio.2023.12.019.

Li, L., Li, S., Gao, H., Chen, C.Q., 2025. ENNStressNet: An unsupervised equilibrium-based neural network for end-to-end stress mapping in elastoplastic solids. J. Mech. Phys. Solids 200, 106117. doi:10.1016/j.jmps.2025.106117.

Liu, W., Tang, J., Jiang, Y., Mao, Y., Hou, S., 2025. Sloppiness of auto-discovered constitutive models for skeletal muscle. Acta Mech. Sin. 41, 624430. doi:10.1007/s10409-024-24430-x.

Melnikov, A., Ogden, R.W., Dorfmann, L., Merodio, J., 2021. Bifurcation analysis of elastic residually-stressed circular cylindrical tubes. Int. J. Solids Struct. 226–227, 111062. doi:10.1016/j.ijsolstr.2021.111062.

Merodio, J., Ogden, R.W., 2016. Extension, inflation and torsion of a residually stressed circular cylindrical tube. Continuum Mech. Thermodyn. 28, 157–174. doi:10.1007/s00161-015-0411-z.

Merodio, J., Ogden, R.W., Rodriguez, J., 2013. The influence of residual stress on finite deformation elastic response. Int. J. Non-Linear Mech. 56, 43–49. doi:10.1016/j.ijnonlinmec.2013.02.010.

Molinari, L., Gerardo-Giorda, L., Gizzi, A., 2022. A transversely isotropic thermo-hyperelastic constitutive model of myocardial tissue with a three-state cell death dynamics for cardiac radiofrequency ablation. J. Mech. Phys. Solids 161, 104810. doi:10.1016/j.jmps.2022.104810.

Mukherjee, S., Destrade, M., Gower, A.L., 2022. Representing the stress and strain energy of elastic solids with initial stress and transverse texture anisotropy. Proc. R. Soc. A 478, 20220255.

Mukherjee, S., Ravindran, P., 2024. Representation of stress and free energy for a viscoelastic body from a stressed reference. J. Mech. Phys. Solids 184, 105544.

Ogden, R.W., 2023. Change of reference configuration in nonlinear elasticity: Perpetuation of a basic error. Mathematics and Mechanics of Solids 28, 2132–2138. doi:10.1177/10812865221141375.

Ogden, R.W., Singh, B., 2014. The effect of rotation and initial stress on the propagation of waves in a transversely isotropic elastic solid. Wave Motion 51, 1108–1126.

Pandolfi, A., 2020. Cornea modelling. Eye Vis. 7, 2.

Pandolfi, A., Holzapfel, G.A., 2008. Three-dimensional modeling and computational analysis of the human cornea considering distributed collagen fibril orientations. J. Biomech. Eng. 130, 061006.

Prume, E., Reese, S., Ortiz, M., 2023. Model-free data-driven inference in computational mechanics. Comput. Methods Appl. Mech. Eng. 403, 115704. doi:10.1016/j.cma.2022.115704.

PyTorch Team, 2024. PyTorch Documentation. PyTorch. Https://pytorch.org/docs/stable/index.html.

Rausch, M.K., Kuhl, E., 2013. On the effect of prestrain and residual stress in thin biological membranes. J. Mech. Phys. Solids 61, 1955–1969. doi:10.1016/j.jmps.2013.04.004.

Reina, C., Conti, S., 2017. Incompressible inelasticity as an essential ingredient for the validity of the kinematic decomposition F=FeFi. J. Mech. Phys. Solids 107, 322–342. doi:10.1016/j.jmps.2017.07.004.

Reina, C., Fokoua Djodom, L.F., Ortiz, M., Conti, S., 2018. Kinematics of elasto-plasticity: Validity and limits of applicability of F=FeFp for general three-dimensional deformations. J. Mech. Phys. Solids 121, 99–113. doi:10.1016/j.jmps.2018.07.006.

Sadik, S., Yavari, A., 2024. Nonlinear anisotropic viscoelasticity. J. Mech. Phys. Solids 182, 105461. doi:10.1016/j.jmps.2023.105461.

Shams, M., Destrade, M., Ogden, R.W., 2011. Initial stresses in elastic solids: Constitutive laws and acoustoelasticity. Wave Motion 48, 552–567.

Shariff, M.H.B.M., Bustamante, R., Merodio, J., 2017. On the spectral analysis of residual stress in finite elasticity. IMA J. Appl. Math. 82, 656–680. doi:10.1093/imamat/hxx007.

Shariff, M.H.B.M., Bustamante, R., Merodio, J., 2019. A nonlinear electro-elastic model with residual stresses and a preferred direction. Math. Mech. Solids 25, 838–865. doi:10.1177/1081286519891769.

Shariff, M.H.B.M., Merodio, J., 2020. Residually stressed two fibre solids: A spectral approach. Int. J. Eng. Sci. 148, 103205.

Skalak, R., Zargaryan, S., Jain, R.K., Netti, P.A., Hoger, A., 1996. Compatibility and the genesis of residual stress by volumetric growth. J. Math. Biol. 34, 889–914. doi:10.1007/BF01834825.

Soyarslan, C., Bargmann, S., 2016. Thermomechanical formulation of ductile damage coupled to nonlinear isotropic hardening and multiplicative viscoplasticity. J. Mech. Phys. Solids 91, 334–358. doi:10.1016/j.jmps.2016.03.002.

Thakolkaran, P., Teichtmeister, M., Balzani, D., 2022. NN-EUCLID: Deep-learning hyperelasticity without stress data. J. Mech. Phys. Solids 169, 105076.

Todd, R., Boccaccini, A., Sinclair, R., Yallee, R., Young, R., 1999. Thermal residual stress and their toughening effect in Al2O3 platelet reinforced glass. Acta Mater. 47, 3233–3240.

Wu, X., Zhang, Y., Mao, S., 2025. Learning the physics-consistent material behavior from measurable data via PDE-constrained optimization. Comput. Methods Appl. Mech. Eng. 437, 117748.

Yan, S., Hu, X., Song, X., Yao, K., Qu, S., 2026. Intraocular pressure prediction method combining finite element simulations and multi-layer perceptron neural network. Acta Mech. Sin. 42, 624940. doi:10.1007/s10409-025-24940-x.

Yang, F., Li, Y., Zhang, K., 2023. A multiplicative finite strain deformation for diffusion-induced stress: An incremental approach. Int. J. Eng. Sci. 187, 103841. doi:10.1016/j.ijengsci.2023.103841.

Yavari, A., Sozio, F., 2023. On the direct and reverse multiplicative decompositions of deformation gradient in nonlinear anisotropic anelasticity. J. Mech. Phys. Solids 170, 105101. doi:10.1016/j.jmps.2022.105101.

Zheng, S., Banerji, R., LeBourdais, R., Zhang, S., DuBois, E., O'Shea, T., Nia, H.T., 2024. Alteration of mechanical stresses in the murine brain by age and hemorrhagic stroke. PNAS Nexus 3, pgae141.

Appendix A. Network Architecture and Specifications

In this study, we employ a fully connected feed-forward neural network consisting of L layers, including an input layer, an output layer, and $L-2$ hidden layers ($L > 2$). Let N_l denote the number of neurons in the l-th layer for $l = 1, 2, \ldots, L$. Specifically, the network comprises $L = 5$ layers, with 400 neurons in each hidden layer ($N_l = 400$ for $l = 2, 3, 4$). The network is trained using the Adam optimizer with a learning rate of 1×10^{-4}, and a batch size of 64.

When constructing constitutive models using neural networks, it is desirable to incorporate physically motivated constraints into the network architecture. In this work, we employ an Input Convex Neural Network (ICNN) to impose convexity of the strain-energy density W with respect to the selected invariant inputs. According to the literature (Klein et al., 2022), a neural network is an ICNN if the following conditions are satisfied: (1) the activation function of every layer is convex and non-decreasing; and (2) all weights, except those in the first layer, are non-negative. We choose the Softplus activation function, which satisfies both requirements. The non-negative-weight constraint is enforced through a positive reparameterization, ensuring that the weights beyond the first layer remain non-negative throughout training.

It should be noted, however, that convexity of W with respect to the invariant inputs does not, in general, guarantee convexity, polyconvexity, or rank-one convexity of W with respect to the deformation gradient $\boldsymbol{F}$. This distinction is particularly important here because some of the invariants used as network inputs are nonlinear functions of $\boldsymbol{C}$ and involve the initial stress $\boldsymbol{\tau}$. Therefore, in the present work, the ICNN architecture is regarded as a physically motivated means of promoting convexity in the invariant space, rather than as a theoretical guarantee of material stability or ellipticity with respect to $\boldsymbol{F}$.

To quantitatively assess the stability of the trained constitutive model, we further evaluated the acoustic tensor

$$Q_{ik} = \mathcal{C}_{ijkl} n_j n_l, \qquad \mathcal{C}_{ijkl} = \frac{\partial^2 W}{\partial F_{ij} \partial F_{kl}},$$

using automatic differentiation. For each unit propagation direction $\boldsymbol{n}$, the acoustic tensor was projected onto the plane perpendicular to $\boldsymbol{n}$, corresponding to the admissible perturbation subspace for the incompressibility constraint. The two eigenvalues of the resulting transverse acoustic tensor $\bar{\boldsymbol{Q}}(\boldsymbol{n})$ were then evaluated for all 200,000 samples in the training dataset. Equivalently, we examined the condition

$$m_i Q_{ik}(\boldsymbol{n}) m_k > 0, \qquad |\boldsymbol{m}| = |\boldsymbol{n}| = 1, \qquad \boldsymbol{m} \cdot \boldsymbol{n} = 0,$$

over the sampled propagation directions and all testing states. For the neo-Hookean constitutive model, the minimum normalized transverse acoustic eigenvalue, $\lambda_{\min}(\bar{\boldsymbol{Q}})/\mu$, over all evaluated samples was 0.1269, and no violation of strong ellipticity was observed.

The transformation from an input $\boldsymbol{x} \in \mathbb{R}^m$ to an output $\boldsymbol{y} \in \mathbb{R}^n$ is defined as

$$\begin{cases} \hat{\boldsymbol{x}}^{(1)} = \boldsymbol{x}, \\ \hat{\boldsymbol{x}}^{(l)} = \text{Softplus}\left(\boldsymbol{W}^l \hat{\boldsymbol{x}}^{(l-1)} + \boldsymbol{b}^l\right), \quad 1 < l < L, \\ \boldsymbol{y} = \boldsymbol{W}^L \hat{\boldsymbol{x}}^{(L-1)} + \boldsymbol{b}^L, \end{cases} \tag{A.1}$$

where $\boldsymbol{W}^l \in \mathbb{R}^{N_l \times N_{l-1}}$ and $\boldsymbol{b}^l \in \mathbb{R}^{N_l}$ are the weight matrix and bias vector of the l-th layer, respectively (note that the input layer has no weights or biases). The Softplus activation function is defined as $\ln(1 + e^x)$. The weights and biases are optimized during training using the backpropagation algorithm to minimize the loss function $\mathcal{L}$.

To determine an appropriate value of the weighting parameter λ, we considered both the training performance and the convergence rate of the neural network. Several values of λ were tested, and

their effects on the training process were compared. Based on a balance between training accuracy and convergence speed, $\lambda = 0.01$ was selected for the present study. The sensitivity of the training results to λ is shown in Fig. A1.

For the training dataset, random material parameters were selected for each constitutive model, together with 20,000 randomly sampled deformation gradients $\boldsymbol{F}_2$. For each $\boldsymbol{F}_2$, 10 different isochoric decompositions into $\boldsymbol{F}$ and $\boldsymbol{F}_1$ were generated to augment the training data and enforce the ISRI condition, resulting in a total of 200,000 augmented samples. All decompositions of the same current configuration were assigned to either the training set or the test set to prevent data leakage. Consequently, the dataset contains a broad range of deformation states, including triaxial and non-coaxial deformations as well as combined loading states. To ensure that the neural network retains accuracy under both large and small deformations—particularly important for wave-propagation problems—the dataset was divided into 125,000 large-deformation samples and 75,000 small-deformation samples. For the small-deformation cases, the deformation gradient tensor $\boldsymbol{F}$ was close to the identity tensor. We reserved 20% of the dataset for testing, while the remaining 80% was used for training. Throughout the training process, the loss decreased by approximately four orders of magnitude. The training results were stable across different random initializations, without requiring a fixed random seed.

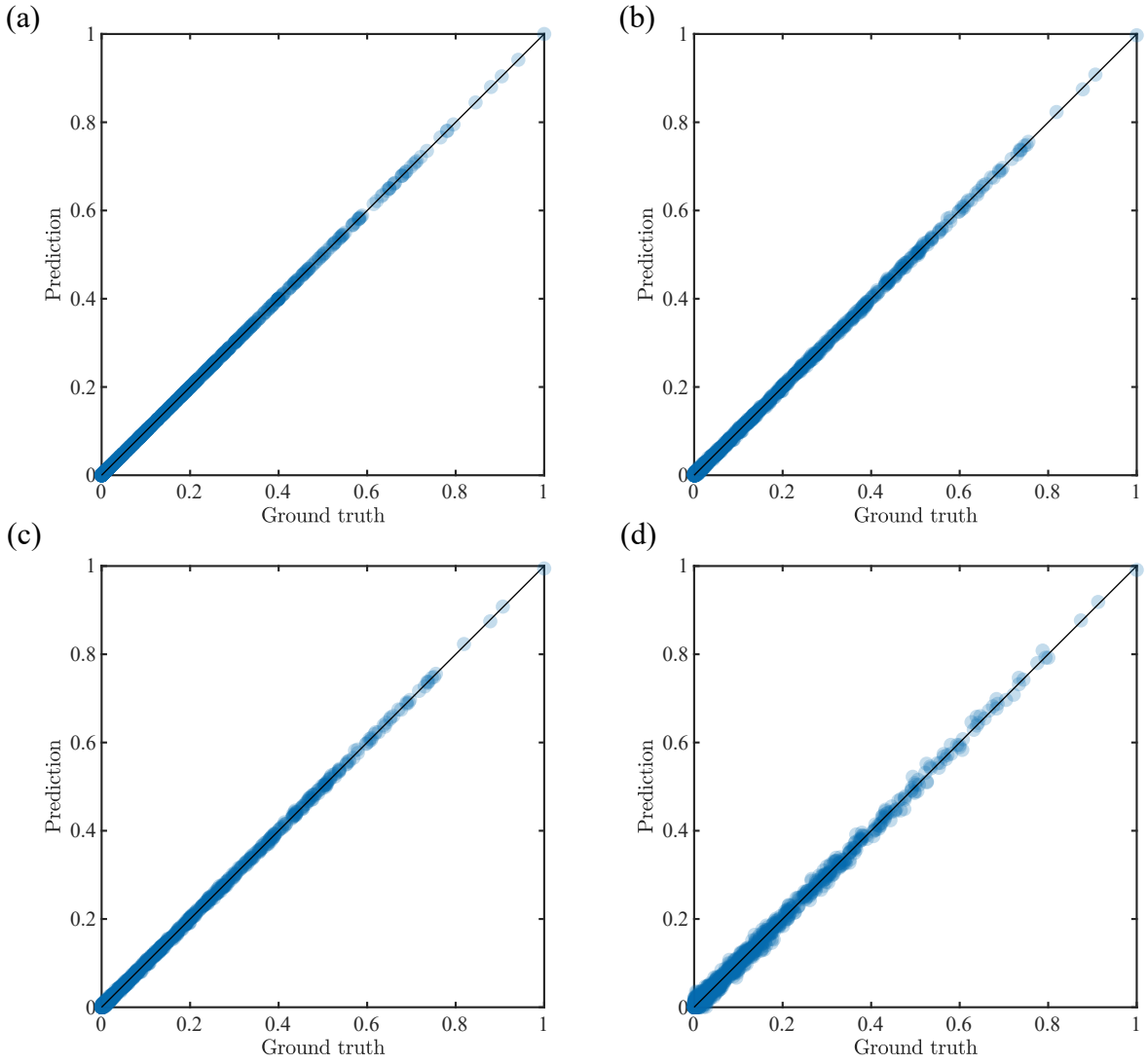


Figure A1: Sensitivity analysis of the neural network training to the weighting parameter λ: (a) $\lambda = 0.01$; (b) $\lambda = 0.001$; (c) $\lambda = 0.05$; and (d) $\lambda = 0.1$.

Appendix B. Training the MINN without strain-energy labels

Figure B1 presents the training results of the MINN using only stress labels. The predictions obtained using only stress labels are nearly indistinguishable from those obtained using both stress and strain-energy labels, indicating that strain-energy labels provide little additional information for the constitutive models considered in this study.

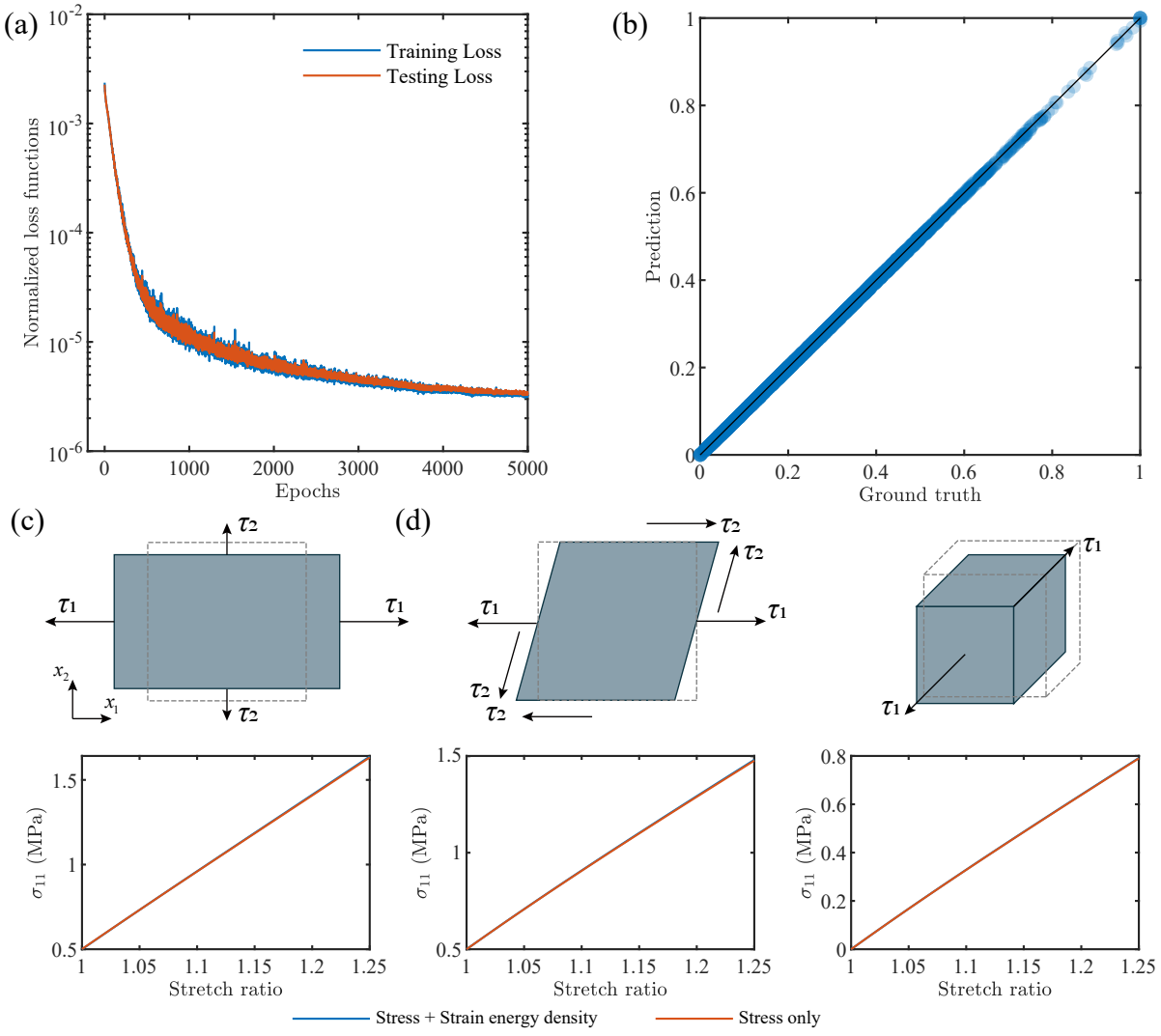


Figure B1: Training performance of the MINN using only stress labels. (a) Evolution of the training and validation losses during optimization. (b) Comparison between the predicted and reference stress values. (c)–(e) Comparison of the stress–stretch responses predicted by the MINN trained using only stress labels and the MINN trained using both stress and strain-energy labels under different initial stress states: (c) in-plane uniaxial stress, (d) in-plane pure shear stress, and (e) out-of-plane uniaxial stress. In all cases, the initial stresses are set to $\tau_1 = 0.5\mu$ and $\tau_2 = 0.3\mu$.

Appendix C. Derivation of the stiffness matrix in the UMAT subroutine

In the UMAT subroutine, the cauchy stress tensors are all in the form of a deviatoric component. The expression for the Cauchy stress is as follows:

$$\begin{aligned}\boldsymbol{\sigma}^{\mathrm{ABA}} = &\frac{2}{J}W_1\left(\bar{\boldsymbol{B}} - \frac{1}{3}\bar{I}_1\mathbf{I}\right) + \frac{2}{J}W_2\left(\bar{I}_1\bar{\boldsymbol{B}} - \bar{\boldsymbol{B}}^2 - \frac{2}{3}\bar{I}_2\mathbf{I}\right) + \frac{2}{J}W_6\bar{\boldsymbol{\Sigma}} \\ &+ \frac{2}{J}W_7\left(\bar{\boldsymbol{\Sigma}}\,\bar{\boldsymbol{B}} + \bar{\boldsymbol{B}}\,\bar{\boldsymbol{\Sigma}}\right) + \frac{2}{J}W_9\left(\bar{\boldsymbol{\Pi}}\,\bar{\boldsymbol{B}} + \bar{\boldsymbol{B}}\,\bar{\boldsymbol{\Pi}}\right),\end{aligned} \tag{C.1}$$

where $\overline{\boldsymbol{\Sigma}} = \overline{\boldsymbol{F}}\boldsymbol{\tau}\overline{\boldsymbol{F}}^T$ and $\overline{\boldsymbol{\Pi}} = \overline{\boldsymbol{F}}\boldsymbol{\tau}^2\overline{\boldsymbol{F}}^T$. The superscript ABA indicates that this is the expression to be used in the UMAT subroutine. $\overline{\boldsymbol{F}} = J^{-1/3}\boldsymbol{F}$, thus we have:

$$\overline{\boldsymbol{B}} = J^{-2/3}\boldsymbol{B}, \quad \overline{\boldsymbol{C}} = J^{-2/3}\boldsymbol{C} \tag{C.2}$$

The expressions for the second-order Piola-Kirchhoff stress $\boldsymbol{P}$ and the Kirchhoff stress $\boldsymbol{T}$ are as follows:

$$\boldsymbol{P} = J\boldsymbol{F}^{-1}\boldsymbol{\sigma}\boldsymbol{F}^{-T}, \quad \boldsymbol{T} = J\boldsymbol{\sigma} \tag{C.3}$$

The stiffness matrix used in the UMAT subroutine is:

$$\boldsymbol{C}^{\mathrm{ABA}} = \frac{1}{J}\frac{\partial\Delta\boldsymbol{T}}{\partial\Delta\boldsymbol{\varepsilon}} = \frac{1}{J}\frac{\partial\Delta\left(J\boldsymbol{\sigma}\right)}{\partial\Delta\boldsymbol{\varepsilon}} \tag{C.4}$$

where J is the determinant of the deformation gradient tensor.

The time derivative of the second-order Piola-Kirchhoff stress can be written as:

$$\dot{\boldsymbol{P}} = 2\frac{\partial\boldsymbol{P}}{\partial\boldsymbol{C}} : \frac{\dot{\boldsymbol{C}}}{2} = \boldsymbol{C}^{\tan} : \frac{\dot{\boldsymbol{C}}}{2} \tag{C.5}$$

The Jaumann-Zaremba rate of the Kirchhoff stress used in the subroutine is:

$$C_{ijkl}^{\mathrm{ABA}} = \frac{1}{J}F_{im}F_{jn}F_{kp}F_{lq}C_{mnpq}^{\tan} + \frac{1}{2}\left(\sigma_{lj}\delta_{ik} + \sigma_{kj}\delta_{il} + \sigma_{ik}\delta_{jl} + \sigma_{il}\delta_{jk}\right) \tag{C.6}$$

where the stiffness matrix relating the rate of change of the second-order Piola-Kirchhoff stress to the rate of strain is:

$$
\begin{aligned}
C^{\tan}_{mnpq} &= 2JW_1\overline{C}^{-1}_{mn}\delta_{pq} + 2JW_2\left(\overline{I}_1\overline{C}^{-1}_{mn}\delta_{pq} - \overline{C}^{-1}_{mn}\overline{C}_{pq}\right) + 2JW_6\overline{C}^{-1}_{mn}\tau_{pq} \\
&+ 2JW_7\left(\overline{C}^{-1}_{mn}\tau_{pa}\overline{C}_{aq} + \overline{C}^{-1}_{mn}\overline{C}_{pa}\tau_{aq}\right) + 2JW_9\left(\overline{C}^{-1}_{mn}\tau_{pa}\tau_{ab}\overline{C}_{bq} + \overline{C}^{-1}_{mn}\overline{C}_{pa}\tau_{ab}\tau_{bq}\right) \\
&+ 4J^{1/3}W_2\left(\delta_{mn}\delta_{pq} - \delta_{mp}\delta_{nq}\right) + 4J^{1/3}W_7\left(\tau_{mn}\overline{C}_{pq} + \overline{C}_{mn}\tau_{pq}\right) \\
&+ 4J^{1/3}W_9\left(\tau_{ma}\tau_{an}\overline{C}_{pq} + \overline{C}_{mn}\tau_{pa}\tau_{aq}\right) + 8J^{-1/3}W_{96}\left(\tau_{mn}\tau_{pa}\tau_{ab}\overline{C}_{bq} + \tau_{mn}\overline{C}_{pa}\tau_{ab}\tau_{bq}\right) \\
&+ 8J^{-1/3}W_{11}\delta_{mn}\delta_{pq} + 8J^{-1/3}W_{12}\left(\overline{I}_1\delta_{mn}\delta_{pq} - \overline{C}_{mn}\delta_{pq}\right) + 8J^{-1/3}W_{16}\tau_{mn}\delta_{pq} \\
&+ 8J^{-1/3}W_{17}\left(\tau_{ma}\overline{C}_{an}\delta_{pq} + \overline{C}_{ma}\tau_{an}\delta_{pq}\right) + 8J^{-1/3}W_{19}\left(\tau_{ma}\tau_{ab}\overline{C}_{bn}\delta_{pq} + \overline{C}_{ma}\tau_{ab}\tau_{bn}\delta_{pq}\right) \\
&+ 8J^{-1/3}W_{21}\left(\overline{I}_1\delta_{mn}\delta_{pq} - \delta_{mn}\overline{C}_{pq}\right) + 8J^{-1/3}W_{99}\left(\tau_{ma}\tau_{ab}\overline{C}_{bn}\overline{C}_{pc}\tau_{cd}\tau_{dq} + \overline{C}_{ma}\tau_{ab}\tau_{bn}\overline{C}_{pc}\tau_{cd}\tau_{dq}\right) \\
&+ 8J^{-1/3}W_{22}\left(\overline{I}^2_1\delta_{mn}\delta_{pq} - \overline{I}_1\overline{C}_{mn}\delta_{pq} - \overline{I}_1\delta_{mn}\overline{C}_{pq} + \overline{C}_{mn}\overline{C}_{pq}\right) \\
&+ 8J^{-1/3}W_{26}\left(\overline{I}_1\tau_{mn}\delta_{pq} - \tau_{mn}\overline{C}_{pq}\right) + 8J^{-1/3}W_{76}\left(\tau_{mn}\tau_{pa}\overline{C}_{aq} + \tau_{mn}\overline{C}_{pa}\tau_{aq}\right) \\
&+ 8J^{-1/3}W_{27}\left(\overline{I}_1\tau_{ma}\overline{C}_{an}\delta_{pq} + \overline{I}_1\overline{C}_{ma}\tau_{an}\delta_{pq} - \tau_{ma}\overline{C}_{an}\overline{C}_{pq} - \overline{C}_{ma}\tau_{an}\overline{C}_{pq}\right) \\
&+ 8J^{-1/3}W_{29}\left(\overline{I}_1\tau_{ma}\tau_{ab}\overline{C}_{bn}\delta_{pq} + \overline{I}_1\overline{C}_{ma}\tau_{ab}\tau_{bn}\delta_{pq} - \tau_{ma}\tau_{ab}\overline{C}_{bn}\overline{C}_{pq} - \overline{C}_{ma}\tau_{ab}\tau_{bn}\overline{C}_{pq}\right) \\
&+ 8J^{-1/3}W_{61}\delta_{mn}\tau_{pq} + 8J^{-1/3}W_{62}\left(\overline{I}_1\delta_{mn}\tau_{pq} - \overline{C}_{mn}\tau_{pq}\right) + 8J^{-1/3}W_{66}\tau_{mn}\tau_{pq} \\
&+ 8J^{-1/3}W_{67}\left(\tau_{ma}\overline{C}_{an}\tau_{pq} + \overline{C}_{ma}\tau_{an}\tau_{pq}\right) + 8J^{-1/3}W_{69}\left(\tau_{ma}\tau_{ab}\overline{C}_{bn}\tau_{pq} + \overline{C}_{ma}\tau_{ab}\tau_{bn}\tau_{pq}\right) \\
&+ 8J^{-1/3}W_{71}\left(\delta_{mn}\tau_{pa}\overline{C}_{aq} + \delta_{mn}\overline{C}_{pa}\tau_{aq}\right) + 8J^{-1/3}W_{91}\left(\delta_{mn}\tau_{pa}\tau_{ab}\overline{C}_{bq} + \delta_{mn}\overline{C}_{pa}\tau_{ab}\tau_{bq}\right) \\
&+ 8J^{-1/3}W_{72}\left(\overline{I}_1\delta_{mn}\tau_{pa}\overline{C}_{aq} - \overline{C}_{mn}\tau_{pa}\overline{C}_{aq} + \overline{I}_1\delta_{mn}\overline{C}_{pa}\tau_{aq} - \overline{C}_{mn}\overline{C}_{pa}\tau_{aq}\right) \\
&+ 8J^{-1/3}W_{77}\left(\tau_{ma}\overline{C}_{an}\tau_{pc}\overline{C}_{cq} + \overline{C}_{ma}\tau_{an}\tau_{pc}\overline{C}_{cq} + \tau_{ma}\overline{C}_{an}\overline{C}_{pc}\tau_{cq} + \overline{C}_{ma}\tau_{an}\overline{C}_{pc}\tau_{cq}\right) \\
&+ 8J^{-1/3}W_{79}\left(\tau_{ma}\tau_{ab}\overline{C}_{bn}\tau_{pc}\overline{C}_{cq} + \overline{C}_{ma}\tau_{ab}\tau_{bn}\tau_{pc}\overline{C}_{cq} + \tau_{ma}\tau_{ab}\overline{C}_{bn}\overline{C}_{pc}\tau_{cq} + \overline{C}_{ma}\tau_{ab}\tau_{bn}\overline{C}_{pc}\tau_{cq}\right) \\
&+ 8J^{-1/3}W_{92}\left(\overline{I}_1\delta_{mn}\tau_{pa}\tau_{ab}\overline{C}_{bq} - \overline{C}_{mn}\tau_{pa}\tau_{ab}\overline{C}_{bq} + \overline{I}_1\delta_{mn}\overline{C}_{pa}\tau_{ab}\tau_{bq} - \overline{C}_{mn}\overline{C}_{pa}\tau_{ab}\tau_{bq}\right) \\
&+ 8J^{-1/3}W_{97}\left(\tau_{ma}\overline{C}_{an}\tau_{pc}\tau_{cd}\overline{C}_{dq} + \overline{C}_{ma}\tau_{an}\tau_{pc}\tau_{cd}\overline{C}_{dq} + \tau_{ma}\overline{C}_{an}\overline{C}_{pc}\tau_{cd}\tau_{dq} + \overline{C}_{ma}\tau_{an}\overline{C}_{pc}\tau_{cd}\tau_{dq}\right) \\
&+ 8J^{-1/3}W_{99}\left(\tau_{ma}\tau_{ab}\overline{C}_{bn}\tau_{pc}\tau_{cd}\overline{C}_{dq} + \overline{C}_{ma}\tau_{ab}\tau_{bn}\tau_{pc}\tau_{cd}\overline{C}_{dq}\right)
\end{aligned}
\tag{C.7}
$$

Appendix D. The properties of the PDMS material used in the experiment

The uniaxial tensile stress–strain curve of the PDMS material used in the experiments is shown in Fig. D1. The plotted curve represents the average response obtained from four measurements on different specimens, for which the identified shear moduli range from approximately 47 to 62 kPa, with an average value of approximately 55 kPa. A linear fit to the averaged stress–strain curve yields a shear modulus of $\mu \approx 55$ kPa, which is slightly higher than the value identified by the proposed method. The observed variation in shear modulus among the specimens is likely associated with differences in cross-linking density among the PDMS specimens. Because the tensile and OCE measurements were performed on different specimens, the difference between the corresponding shear moduli cannot be directly interpreted as the identification error of the proposed method. In addition, the assumed density used in the analysis also affects the identified shear modulus: varying the assumed density from 800 to 1200 kg/m^3 results in shear moduli ranging from 35.43 to 52.86 kPa, compared with 44.16 kPa obtained using the assumed density of 1000 kg/m^3.

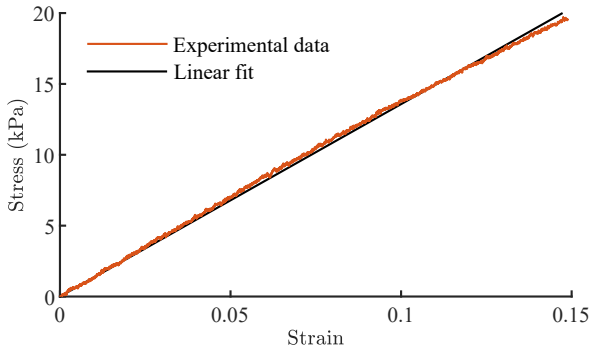


Figure D1: Average uniaxial tensile stress–strain curve measured for the PDMS material used in the experiments.

Appendix E. Quantitative Verification of the ISRI Condition

To quantitatively verify the initial stress reference independence (ISRI) condition, we consider the same current configuration $\boldsymbol{F}_2$ represented by two different decompositions,

$$\boldsymbol{F}_2 = \boldsymbol{F}\boldsymbol{F}_1 = \hat{\boldsymbol{F}}\left(\bar{\boldsymbol{F}}\boldsymbol{F}_1\right). \tag{E.1}$$

The ISRI verification was performed using an independent set of configurations that were not used for training or data augmentation. Specifically, the current configurations $\boldsymbol{F}_2$ and the corresponding decompositions were newly sampled and were independent of those used to construct the training dataset.

According to the ISRI condition, these different decompositions correspond to different initially stressed reference configurations but must yield the same strain-energy density for the same current configuration. We therefore evaluate the predicted strain-energy densities for the two decompositions and compare $W\left(\boldsymbol{F}, \boldsymbol{\tau}\right)$ and $W\left(\hat{\boldsymbol{F}}, \bar{\boldsymbol{\tau}}\right)$.

The results are shown in Fig. E1. The strain-energy densities obtained from the two different decompositions exhibit close agreement over the tested samples, the resulting maximum normalized ISRI residual was 2.6472×10^{-4}, demonstrating that the learned constitutive model satisfies the ISRI condition to a high degree of accuracy. This quantitative verification further confirms that the data augmentation strategy based on multiple decompositions of the same current configuration is consistent with the reference-independence requirement.

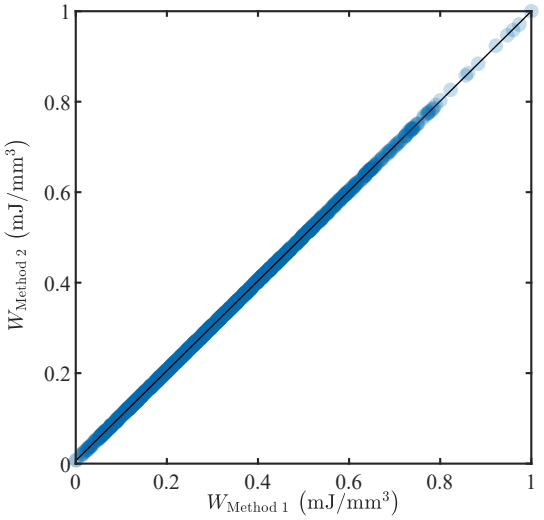


Figure E1: Quantitative verification of the ISRI condition by comparing the strain-energy densities obtained from two different decompositions of the same current configuration.